Revision 2 (Manuscript 6056R)
Resubmitted to American Mineralogist on April 27th 2017

Trace element inventory of meteoritic Ca-phosphates

Dustin Ward[1], Addi Bischoff[1], Julia Roszjar[2], Jasper Berndt[3] and Martin J. Whitehouse[4]

[1]Institut für Planetologie, Westfälische Wilhelms-Universität Münster, Wilhelm-Klemm-Str. 10, 48149 Münster, Germany
[2]Department of Mineralogy and Petrography, Natural History Museum Vienna, Burgring 7, 1010 Vienna, Austria
[3]Institut für Mineralogie, Westfälische Wilhelms-Universität Münster, Corrensstraße 24, 48149 Münster, Germany
[4]Department of Geosciences, Swedish Museum of Natural History, Box 50007, 10405 Stockholm, Sweden

Abstract

Most extraterrestrial samples feature the two accessory Ca-phosphates - apatite-group minerals and merrillite, which are important carrier phases of the rare earth elements (REE). The trace element concentrations (REE, Sc, Ti, V, Cr, Mn, Co, As, Rb, Sr, Y, Zr, Nb, Ba, Hf, Ta, Pb, Th and U) of selected grains were analyzed by LA-ICP-MS and/or SIMS (REE only). This systematic investigation includes 99 apatite and 149 merrillite analyses from meteorites deriving from various asteroidal bodies including one carbonaceous chondrite, eight ordinary chondrites, three acapulcoites, one winonaite, two eucrites, five shergottites, one ureilitic trachyandesite, two mesosiderites and one silicate-bearing IAB iron meteorite.

Although Ca-phosphates predominantly form in metamorphic and/or metasomatic reactions, some are of igneous origin. As late-stage phases that often incorporate the vast majority of their host's bulk REE budget, the investigated Ca-phosphates have REE enrichments of up to two orders of magnitude compared to the host rocks bulk concentrations. Within a single sample, each phosphate species displays a uniform REE-pattern, and variations are mainly restricted to their enrichment, therefore indicating similar formation conditions. Exceptions are brecciated samples, i.e., the Adzhi-Bogdo (LL3-6) ordinary chondrite. Despite this uniformity within single samples, distinct meteorite groups do not necessarily have unique REE-patterns. Four basic shapes dominate the REE patterns

of meteoritic Ca-phosphates: (1) Flat patterns, smoothly decreasing from La-Lu with prominent negative Eu anomalies (acapulcoites, eucrites, apatite from the winonaite and the ureilitic trachyandesite, merrillite from ordinary chondrites); (2) unfractionated patterns, with only minor or no anomalies (mesosiderites, enriched shergottites, IAB-iron meteorite); (3) LREE-enriched patterns, with either positive or slightly negative Eu anomalies (chondritic apatite); and (4) strongly LREE-depleted patterns, with negative Eu anomalies (depleted shergottites). The patterns do not correlate with the grade of metamorphism (petrologic type), specific adjacent mineral assemblages or with Ca-phosphate grain size. Neither the proportions of different REE, nor particular REE patterns themselves are universally correlated to a specific formation mechanism yet Eu (i.e., magnitude of the Eu anomaly) is a sensitive indicator to evaluate the timing of plagioclase and phosphate crystallization. Based on our data, U and Th abundances in apatite increase (almost linearly) with the grade of metamorphism, as well as with the differentiation of their host rock.

Keywords

Meteorites, apatite, merrillite, Ca-phosphates, trace elements, REE, LA-ICP MS, SIMS

This is a preprint, the final version is subject to change, of the American Mineralogist (MSA)
Cite as Authors (Year) Title. American Mineralogist, in press.
(DOI will not work until issue is live.) DOI: http://dx.doi.org/10.2138/am-2017-6056

Introduction

Although Ca-phosphates are only accessory phases in numerous meteorite classes, they are ubiquitous and represent the predominant phosphorous (P) reservoir in meteorites. The most common meteoritic Ca-phosphate species are apatite-group minerals [$Ca_5(PO_4)_3(F,Cl,OH)$] (later referred to as apatite) and merrillite [$Ca_9NaMg(PO_4)_7$], with the latter being devoid of hydrogen with respect to the predominantly terrestrial whitlockite [$Ca_9Mg(PO_4)_6(PO_3OH)$] (e.g., Hughes et al. 2008). Although both terms, whitlockite and merrillite, are still often used interchangeably in descriptions of extraterrestrial material, we concur with Rubin (1997) and Jones et al. (2014) and refer to the anhydrous Na- and Mg-bearing Ca-phosphate phase within our sample suite as merrillite. However, a (hydrated) whitlockite component, especially in Martian meteorites, cannot be excluded (Shearer et al. 2015). Detailed chemical and structural information on merrillite is given i.e. by Jolliff et al. (1993, 2006), Hughes et al. (2008), and Xie et al. (2015).

This study focusses on meteoritic apatite and merrillite deriving from diverse asteroidal bodies in the inner Solar System. Both species occur in varying abundances and their grain sizes range from a few micrometers to millimeters. They usually coexist, but one or the other may be absent in some samples. While both phases are considered to be of metamorphic origin in (most) chondrites (Brearley and Jones 1998; Jones et al. 2014) and many differentiated meteorites (e.g. Crozaz et al. 1985; Davis and Olsen 1991), an igneous origin has been inferred for Ca-phosphates from some meteorite groups or individual samples, e.g. eucrites (Delaney 1982, 1984a, 1984b), shergottites (McCubbin et al. 2012; Sarafian et al. 2013, 2017; Shearer et al. 2015), the ureilitic trachyandesite ALM-A (Bischoff et al. 2014), as well as (at least) some of the phosphates in pallasites (Davis and Olsen 1991) and lunar rocks (Delaney 1984b). Ca-phosphates are common accessory phases in lunar meteorites and a major source of volatiles in these rocks (e.g., Joy et al. 2014; Boyce et al. 2014, and refs therein). However, the severe brecciation and overprint by shock, igneous activity and/or even

aqueous alteration in lunar meteorites and rocks might obscure primary mineral parageneses and prevents the exact assignment of phosphates to their original source lithologies in many cases.

The formation of metamorphic Ca-phosphates in chondrites is assumed to be initiated with the oxidation of phosphorous initially located in chondrules or dissolved in Fe,Ni-metal, which then reacts with surrounding silicates (olivine, pyroxene, etc.) to form the phosphates (Brearley and Jones 1998; Jones et al. 2014). Moreover, a metasomatic contribution to Ca-phosphate formation during metamorphism is discussed for some ordinary chondrites (Jones et al. 2014, 2016; Lewis and Jones 2016). Since igneous phosphates are formed late within the crystallization sequence of their parent melt (Delaney 1984b; Davis and Olsen 1991; Shearer et al. 2015), they may incorporate high amounts of incompatible trace elements, especially the rare earth elements (REEs), U and Th.

Although Ca-phosphates occur only as accessory phases (most meteorites do not exceed 1 vol% of both phosphate species combined), they are, if present, important and often the dominant carrier phases for the REEs, as well as for halogens (F, Cl, Br, I) and hydrogen. Halogens are predominately incorporated in apatite, although merrillite is also capable of incorporating minor amounts of F and Cl (e.g., McCubbin et al. 2014). If apatite occurs, its halogen content usually reflects that of the bulk host sample (e.g., Roszjar et al. 2013) and therefore igneous apatite is frequently examined to gain insight into the volatile evolution of planetary bodies; e.g. Mars (Bellucci et al. 2016), the Moon (Boyce et al. 2014) or the parent body of the howardite-eucrite-diogenite (HED) suite of meteorites (Sarafian et al. 2013, 2017). Furthermore, it is also often used to establish constraints on the composition and evolution of the magma from which it has crystallized (e.g., Jolliff et al. 1993, Patiño-Douce and Roden 2006; Patiño-Douce et al. 2011; McCubbin et al. 2010, 2011, 2014; Gross et al. 2013; Sarafian et al. 2013, 2017). Since chondrites have not been melted since their accretion (despite heating to varying degrees), their REE budget is not altered by secondary fractionation which enables their use for constraining processes in the early Solar System.

In differentiated meteorites the REE provide clues for igneous fractionation processes affecting the parent body and enable constraints on its magmatic evolution.

Numerous investigations have examined the extremely high concentrations of REE in meteoritic phosphates – in eucrites they exhibit enrichments of up to 30,000 × CI (Delaney et al. 1984b). These investigations have covered both chondritic (e.g., Van Schmus and Ribbe 1969; Ebihara and Honda 1983; Reed et al. 1983; Reed and Smith 1984; Crozaz and Zinner 1985; Crozaz et al. 1989) and achondritic samples (Delaney 1982; Delaney et al. 1984a, 1984b; Laul and Smith 1986; Davis et al. 1993; Zipfel et al. 1995; Hsu and Crozaz 1996; Shearer et al. 2015). Overall, Ca-phosphates provide valuable insight into the genesis and evolution of their host rocks. Nevertheless, their abundances, distribution and formation mechanisms remain poorly constrained. Therefore, we present a survey of occurrences, phase associations, mineralogy, and trace element chemistry of apatite and merrillite in a comprehensive dataset extending over twelve asteroidal meteorite (sub)groups. Preliminary data on the sample suite discussed here has been published in Ward et al. (2014, 2015, 2016).

Material and Analytical Methods

The analyzed thin sections are part of the meteorite collection at the Institut für Planetologie of the Westfälische Wilhelms-Universität (WWU) Münster, Germany; the meteorites and thin section numbers are given in Table 1. Despite their rarity in some meteorite groups, over 600 Ca-phosphate grains were documented chemically and petrographically. The trace element concentration – with particular emphasis on the REEs – of selected grains was analyzed by laser ablation inductively coupled plasma mass spectrometry (LA-ICP-MS) at the University of Münster (Germany) and/or secondary ion mass spectrometry (SIMS) at the NordSIMS Laboratory in Stockholm (Sweden). This dataset covers ordinary chondrites, a carbonaceous chondrite, acapulcoites, eucrites, shergottites, winonaites, mesosiderites, as well as a IAB iron meteorite and an ureilitic trachyandesite (Table 1).

Scanning Electron Microscopy

A JEOL 6610-LV electron microscope (SEM) at the WWU Münster was used to locate, identify and document the Ca-phosphates and the parageneses with which they are associated. The chemical characterizations of the different mineral constituents were obtained by an attached EDS system (INCA; Oxford Instruments) operating at 20 kV, while the beam current was controlled by a Faraday cup. The different P-bearing phases were identified by multiple element mappings, each conducted with three frames with a dwell time of 250-950 μs. The reference materials used for semi-quantitative analysis were (Astimex) apatite (P, Ca, F), tugtupite (Cl), olivine (Mg, Fe, Si), jadeite (Na), plagioclase (Al), sanidine (K), rutile (Ti), rhodonite (Mn), chromium oxide (Cr) and pentlandite (Ni).

Electron Microprobe Analysis

Quantitative analyses of the Ca-phosphates were conducted with a JEOL JXA 8900 Superprobe electron microprobe. It was operated at 15 keV accelerating voltage with a defocused beam of 5 μm at a beam current of 15 nA. In total, 15 elements were measured using the following standards: Astimex fluorite (Ca, F), Astimex apatite (P), USNM Rockport fayalite (Fe), USNM San Carlos olivine (Mg), rhodonite (Mn), celestine (Sr, S), jadeite (Na), sanidine (K), hypersthene (Si), Astimex rutile (Ti), kyanite (Al), Astimex chromium oxide (Cr) and Astimex tugtupite (Cl). For apatite, F and Cl concentrations were measured first and exposed to a lower beam current of 5-15 nA to prevent migration or loss of volatiles. Counting times were 10 s on peak and 5 s on background, except for Cl, F, Na and K, which were 7 s on peak and 3.5 s on background. The matrix corrections were made according to the $\Phi\rho(z)$ procedure outlined by Armstrong (1991).

The hydroxyl component in apatite had to be calculated by difference according to atomic proportions based on the number of oxygens and assuming an occupancy of the X-site with two anions, giving a total of $X_{Cl} + X_{F} + X_{OH} = 2$. The calculated OH-fraction of the apatite X-site may

136 therefore also include other anions besides F and Cl (e.g., Br or I) and/or also possible vacancies in
137 the apatite crystal structure. Furthermore the calculated X-site fraction is of course biased by the
138 uncertainties of the obtained Cl and F contents. Detection limits (3 σ above background) and errors
139 are given in Tables 2a and 2b) and listed in supplemental Table S1. Analyses were validated with two
140 reference materials (Durango apatite and one in-house apatite reference material), results are listed in
141 supplemental Table S2.

142 **Laser Ablation Inductively Coupled Plasma Mass Spectrometry**

143 The abundances of 32 trace elements (supplemental Table S1) for Ca-phosphate grains larger
144 than 25 μm were analyzed at the Institut für Mineralogie (WWU Münster) by a *Finnigan Element* 2
145 single collector ICP-MS coupled with Excimer laser ablation system (Analyte G2, Photon Machines).
146 The latter provided an output wavelength of 193 nm and was operated with a fluence of 3 J/cm² and
147 a repetition rate of 5 Hz. Counting times were 40 s on peak signals and 20 s on background
148 respectively. The spot-size was adjusted for each grain depending on its size and condition (e.g.,
149 cracks, inclusions, etc.) and varied from 25–65 μm. Reference material was NIST-SRM 612 glass. For
150 quantification ^{43}Ca was used as internal standard. To keep track of precision and accuracy basaltic
151 BIR-1G (Gladney and Roelandts 1988) and phosphatic STDP5 (Klemme et al. 2008) reference
152 glasses were measured as unknowns over the course of this study. Results are given in supplemental
153 Table S2.

154 **Secondary Ion Mass Spectrometry**

155 The REE concentrations of Ca-phosphates smaller than 25 μm were analyzed by a CAMECA
156 IMS 1280 large geometry ion microprobe at the Swedish Museum of Natural History, Stockholm
157 (NordSIMS laboratory). The analytical protocol corresponds to that described by Lepland and
158 Whitehouse (2011): The ellipsoidal (long axis: ~20 μm) O_2^- primary beam operated with an incident
159 energy of 23 kV. Spot sizes of 5 μm, 7 μm or 20 μm (corresponding beam currents of 0.5 nA, 1 nA

and 13 nA) were chosen according to the shape and size of the grains, using Köhler illuminated apertures in the primary column.

The REE were determined as M^+ ions using an ion-counting electron multiplier by a peak-hopping routine comprising the REE and two apatite matrix peaks, $^{40}Ca_2{}^{31}P^{16}O_3$ and $^{40}Ca_2{}^{31}P^{16}O_4$. Following a 60 second pre-sputter over a rastered area of 25 × 25 μm to remove the Au coating, the beam was centered in the field aperture and secondary ion energy optimized in a 60 eV energy window using the $^{40}Ca_2{}^{31}P^{16}O_3$ species. These steps were followed by mass calibration adjustment using the $^{40}Ca^{31}P^{16}O$, $^{40}Ca_2{}^{31}P^{16}O_3$ ^{139}La, and $^{40}Ca_2{}^{31}P^{16}O_4$ species. The mass spectrometer was set at a mass resolving power (MRP) of ~10,000 (M/ΔM) with a 35-μm entrance slit together with a 122-μm exit slit in order to adequately separate heavy (HREE) ions from those of interfering light REE oxide species. After the centering and beam optimization steps, the data acquisition mass sequence comprised 16 scans with an overall integration time of 120 s. Durango apatite was used as in-house reference material, analyses of which were regularly interspersed with the unknowns. Durango REE concentrations used for normalization are given in the supplemental table S3.

Results

The data obtained are consistent with existing trace element analyses covering the respective meteorite groups (e.g., Delaney et al. 1984b; Crozaz and Zinner, 1985; Crozaz et al. 1989; Davis et al. 1993; Wadhwa et al. 1993; Hsu and Crozaz, 1996; Jones et al. 2014), including a few samples which have been analyzed previously (e.g., Zipfel et al. 1995; Ruzicka et al. 2005; Shearer et al. 2015). Multiple analyses with both methods – LA-ICP-MS and SIMS – were applied on several apatite and merrillite grains within different samples (Devgaon, Villalbeto de la Peña, Acapulco, Northwest Africa (NWA) 5073), all providing consistent results. One representative example is provided in supplementary Figure S1, showing an apatite grain from Acapulco with the location of multiple spots of all applied methods, the corresponding REE data, as well as the range of literature values.

184 **Occurrence and Distribution of Ca-phosphates**

185 Ca-phosphates are ubiquitous, yet accessory minerals within the sample suite, but both species
186 do not necessarily occur together in the same meteorite. In the carbonaceous chondrite Karoonda
187 (CK4), the acapulcoite Dhofar 125 and the winonaite Hammadah al Hamra (HaH) 193, only apatite
188 was observed; whereas in the Allegan H5 ordinary chondrite, the acapulcoite NWA 1052, the
189 depleted shergottites Sayh al Uhaymir (SaU) 005 and Dar al Gani (DaG) 1051, as well as in the
190 mesosiderites Dalgaranga and Bondoc, only merrillite was found (Table 1).

191 **Chondrites**

192 Chondritic Ca-phosphates are predominantly located in two main mineral associations,
193 independent from their host's chondrite class: (1) at metal-sulfide interfaces (Fig. 1) and (2) in
194 parageneses with silicates (Figs. 2-3). They are observed next to or in a few cases also within
195 chondrules or in silicate fragments (Figs. 2-3), within the matrix (Figs. 2c and 3c) or in one case, in
196 contact with a Ca,Al-rich inclusion (CAI; Fig. 2b). However, the occurrence within chondrules and
197 also the direct contact to CAIs is rather uncommon. The dominant assemblages are the metal-sulfide
198 interface and, for higher petrologic types, silicate assemblages in recrystallized areas.

199 (1) Phosphates at the metal-sulfide interface (Fig. 1) are often located adjacent to or, in a few
200 cases, enveloping sulfides and/or Fe-,Ni-metal (Figs. 1a and b). They also occur as inclusions in
201 metal (Fig. 1c), metal-sulfide intergrowths or with iron oxides (e.g. magnetite, Fig. 1d). Apatite in the
202 metal- and sulfide-dominated associations varies in size independently of the chondrite class, ranging
203 from 15 to 350 μm; merrillite tends to reach slightly larger sizes, ranging from 20 to 450 μm. Both
204 species increase in average grain size with higher petrologic types of their host rocks. Both apatite
205 and merrillite usually exhibit subhedral to anhedral shapes, and sometimes contain small inclusions
206 of silicates, metal or sulfides (Fig. 1a).

(2) Assemblages with silicates (predominantly pyroxene, olivine, and plagioclase) are common as well (Fig. 2). Metal or sulfides may be located in the vicinity, but the majority of the anhedral to subhedral phosphate grains are in contact with the silicates (Fig. 2a). In rare cases, both Ca-phosphate species occur intergrown, or may be replaced by each other. In each meteorite sample, the phosphate grain sizes in silicate associations are slightly larger compared with those in phosphate-metal-sulfide assemblages, except for Landes (silicate-bearing IAB iron meteorite) and HaH 193 (winonaite). The H3.8 chondrite Devgaon contains the unique assemblage of a CAI enveloped by several anhedral merrillite grains (Fig. 2b). Within the Karoonda CK4 carbonaceous chondrite, the only Ca-phosphates observed are sub- to anhedral apatite grains with a maximum size of 50 μm, occurring as fragments in contact with low-Ca pyroxene and plagioclase. All phases in this particular assemblage contain tiny inclusions of magnetite (Fig. 2c). Yet merrillite assemblages with pentlandite, troilite and schreibersite have been reported from other subgroups of carbonaceous chondrites (e.g. in CV and CO chondrites by Rubin and Grossman 1985).

The LL3-6 chondritic regolith breccia Adzhi-Bogdo (stone) has different Ca-phosphate bearing lithologies. It is highly metamorphosed, and hence recrystallized petrologic type 6 fragments frequently contain both apatite and merrillite (Figs. 3a-b), with apatite being more abundant than merrillite (Table 1). Ca-phosphates do occur, but are uncommon in the less- metamorphosed fragments and also the fine-grained matrix. Additionally, subhedral to euhedral apatite and merrillite grains are present in differentiated fragments (Fig. 3c-d) with clearly achondritic textures (alkali-granitoids or pyroxene-rich clasts with exsolution features), which have been previously described by Bischoff et al. (1993), Sokol et al. (2007a), and Terada and Bischoff (2009).

Differentiated meteorites

Ca-phosphate-bearing mineral parageneses in achondrites commonly occur interstitial to the major rock-forming silicates, or within the late-crystallizing, incompatible-element enriched

mesostasis areas. They are often more abundant than in chondrites (Table 1). Apatite can reach large grain-sizes of several hundred μm (e.g., Fig. 1c) and the grain shapes are predominantly anhedral to subhedral, except for apatite in two samples: apatite grains in the winonaite HaH 193 tend to be elongated in shape, and the ureilitic trachyandesite ALM-A (Bischoff et al. 2014) contains euhedral, lath-shaped grains coexisting with feldspar and pyroxene (Fig. 2d). The lath sizes are up to 200 μm in their longest dimension. In basaltic eucrites and shergottites, the silicate-dominated assemblages also include ilmenite, a SiO_2-polymorph, as well as frequently observed chromite (Fig. 2e-f). In addition to the typical silicates, chromite and ilmenite occur as small inclusions within both Ca-phosphates (Figs. 2e-f). Merrillite in shergottites consistently exhibits larger grain sizes (mostly 50-500 μm), in rare cases at the millimeter scale (Fig. 2f), while apatite remains in a range of 20-300 μm. Furthermore, the enriched shergottite Ksar Ghilane (KG) 002 features an assemblage of merrillite with symplectites: fine-grained vermicular to microgranulitic textures dominated by intergrowths of fayalite, Ca-pyroxene, and silica (Fig. 2f); a detailed petrographic description is given by Llorca et al. (2013).

Chemical Composition

Tables 2a and 2b give the average major element chemistry of apatite and merrillite for each sample. Individual concentrations in wt%, as well as atoms per formula unit (apfu) and the mole fraction Mg/(Mg+Fe) are provided in the supplementary material (Table S1). Cation abunances were determined according to atomic proportions based on 26 oxygens for apatite ($Ca_5(PO_4)_3(OH,F,Cl)$) and 56 oxygens for merrillite ($Ca_{18}Na_2Mg_2(PO_4)_{14}$). Figure 4 illustrates the observed chemical variations in the FeO, MgO, and Na_2O contents of apatite and merrillite.

Compared to apatite, merrillite has higher concentrations of Mg, Na, and Fe, as these elements are major structural constituents, which show considerable variations (Figs. 4a and c). In most meteorite groups, the merrillite MgO content varies between 3.1 and 3.8 wt%, with a few merrillite

255 grains from the Millbillillie eucrite extending the merrillite range down to 2.82 wt% MgO (Fig. 4a).
256 Merrillite in the enriched shergottites NWA 4864 and Zagami stands out due to its significantly lower
257 MgO (1.89-2.48 wt%) and higher FeO (2.46-3.4 wt%) content compared to those occurring in the
258 depleted subgroup (Fig. 4a). Merrillite from mesosiderites and eucrites has the lowest Na_2O
259 concentration (≤1.1 wt%; Fig. 4c) and the mesosiderite Dalgaranga also has the highest spread in
260 merrillite FeO content (1.58-5.02 wt%; Fig. 4).

261 In apatites, the MgO concentration does not exceed 0.45 wt%, but within each sample
262 variations are only minor. Apatites in specific meteorite groups display distinct chemical ranges:
263 apatite grains in ordinary chondrites, shergottites and eucrites have the lowest MgO contents
264 (≤0.2 wt%), while apatite from the CK carbonaceous chondrite, acapulcoites, the winonaite and the
265 IAB iron meteorite plot in the range of 0.15-0.3 wt% MgO. Apatite with the highest MgO and Na_2O
266 abundances is found in the ureilitic trachyandesite from the Almahata Sitta meteorite breccia (up to
267 0.45 wt% MgO and 0.62 wt% Na_2O; Figs. 4b and d). The remaining apatites plot in two fields of the
268 diagram: Those from most ordinary chondrites and the IAB iron meteorite have Na_2O contents of
269 0.2-0.50 wt%, while apatite from the remaining groups does not exceed 0.25 wt% Na_2O. Only apatite
270 from the Adzhi-Bogdo regolith breccia ranges from 0.13-0.3 wt% Na_2O (Table 3). In some cases, the
271 Na-concentrations are below the detection limit. This is the case for eucrites, the winonaite sample,
272 as well as for some apatite grains from the Karoonda CK chondrite (Table 3). Overall, apatite
273 exhibits considerable variation in its FeO content (Fig. 4b). The spread in FeO is quite large
274 (≥1 wt%) in chondrites (Ybbsitz (H4): 0.36-2.27 wt% and Karoonda (CK4): 0.59-1.76 wt%), and the
275 winonaite HaH 193 (0.14-1.49 wt%). It is much smaller (≤1 wt%) in acapulcoites (0.07-0.85 wt%),
276 shergottites (0.40-0.99 wt%) and eucrites (0.64-1.41 wt%; Fig. 4b).

277 Since OH could not be determined by electron microprobe measurements, it had to be
278 calculated by difference. Therefore, this X-site component may also include other substitutions (e.g.,

279 Br or I; Roszjar et al. 2013) or vacancies in the apatite crystal structure. Furthermore Jones et al.
280 (2014) demonstrated by SIMS measurements that apatite from several LL chondrites is very dry
281 (<96 ppm H_2O), although the calculated difference accounts for up to 26% of the X-Site occupied
282 by the OH ± "other" component. Figure 5 demonstrates the variation of the apatite X-site
283 composition within the analyzed sample suite. Ordinary chondrites contain apatite with the highest
284 Cl content (up to 94% occupancy of the X-site) and also a large variation within their X-site
285 composition, (up to a measured occupation of 40% F). Within literature data, the occupancy extends
286 to 75% F and 65% OH (Patiño-Douce and Roden 2006; Jones et al. 2014; McCubbin and Jones
287 2015; Fig. 5a). These variations do not correlate with the subdivision of the ordinary chondrites into
288 H, L and LL chondrites. Apatite from the carbonaceous chondrites have similar Cl contents, but
289 lower F abundances (14-17% occupation of the X-site) and higher OH ± "other" proportions (up to
290 33% of their X-site; Fig. 5b). Some apatite grains from Karoonda (CK4) extend the previously
291 known compositional range (e.g. Patiño-Douce and Roden 2006; Zhang and Yurimoto 2013; Dyl et
292 al. 2015) towards the F and OH ±"other" fraction (Fig. 5b), however available apatite data for
293 carbonaceous chondrites is limited and often clusters with only one dominating X-site fraction (e.g.
294 Cl for DaG 978; Zhang and Yurimoto 2013) or OH ±"other" in Allende; Dyl et al. 2015).

295 The X-site of apatite from differentiated meteorites has higher F content than in chondritic
296 samples. Apatite from primitive achondrites additionally has a very low OH ± "other" fraction:
297 apatite from acapulcoites does not exceed 7% OH ± "other" occupancy of its X-site (Table 3).
298 Apatite from acapulcoites in this study is F-rich (Fig. 5c), although literature data includes quite a
299 large range of Cl and F occupancy (25-65% and 35-75%, respectively; Patiño-Douce and Roden,
300 2006). Apatite from the winonaite HaH 193 lacks the OH ± "other" component in its X-site and
301 exhibits high F abundances (90-96% X-site occupation; Fig. 5c). The X-site of apatite in the ureilitic
302 trachyandesite ALM-A has a F/Cl value of approximately one (Fig. 5c), while apatite from eucrites

303 predominantly clusters at the F-endmember (up to 97% X-site occupancy), but the OH fraction
304 reaches up to 30% (Fig. 5c). Apatite in Martian meteorites exhibits a large variety in composition of
305 their X-sites (Fig. 5d). Even within a single sample, significant variations exist and they exhibit the
306 highest OH ± "other" content within our sample set.

307 **Trace Element Inventory**

308 **Rare Earth Elements (REE).** Table 3 gives the average REE concentrations for apatite and
309 merrillite from the sample suite studied in this work; individual analyses are provided within the
310 supplementary material (Table S1). The REE appear evenly distributed within individual Ca-
311 phosphate grains, as multiple analyses of the same grains overlap within error, which is illustrated in
312 supplementary Figure S1. Achondritic phosphates generally show significantly higher REE contents
313 compared to chondritic samples (up to 21,000 × CI and up to 300 × CI, respectively; Figs. 6-9). If
314 both species are present, merrillite typically exceeds apatite in its REE enrichment by an order of
315 magnitude (Table 3, Figs. 6-9).

316 Within a single sample, each phosphate species, regardless of its mineral assemblage, typically
317 displays a constant shape of chondrite-normalized REE-pattern, i.e., if variations occur, they are
318 mainly restricted to the REE enrichment and not to the particular shape.

319 **REE in Apatite.** Apatite shows two different principal shapes of REE patterns. In chondrites
320 it has fractionated patterns with either positive or negative Eu anomalies (Fig. 6), while in
321 achondrites it generally has smoothly fractionated patterns with prominent negative Eu anomalies
322 (Fig. 7). In all investigated chondrites, apatite does not exceed an overall REE enrichment of 125 ×
323 CI and shows an enrichment of the LREE (La-Sm) over the HREE (Gd-Lu), with a ratio of La/Lu
324 ≈ 2.6-8.4. However, chondrites show variation with respect to the Eu concentration in apatite.
325 Europium anomalies are given as the ratio between Eu and the calculated value Eu* (interpolation
326 between chondrite-normalized Sm and Gd abundances) expected on a smooth chondrite-normalized

327 plot. While a distinct positive Eu anomaly (Fig. 6a) is observed in apatite from the ordinary
328 chondrites Devgaon (H3.8; Eu/Eu* ≈ 2.14) and Portales Valley (H6; Eu/Eu* ≈ 3.35), a slightly
329 negative Eu anomaly and a slightly higher overall REE enrichment (Fig. 6b) occur in apatite from the
330 ordinary chondrites Ybbsitz (H4; Eu/Eu* ≈ 0.88), Bruderheim (L6; Eu/Eu* ≈ 0.71), and Villalbeto
331 de la Peña (L6; Eu/Eu* ≈ 0.75). The range and slope of the patterns coincide with the apatite REE
332 data reported by Crozaz et al. (1989; Figs. 6a and b), yet previous data only included negative Eu
333 anomalies. Apatite from the carbonaceous chondrite Karoonda (CK4) does not show a Eu anomaly,
334 but has slightly elevated CI-normalized abundances of Ce and Pr compared to the remaining REE
335 (Fig. 6c). Within the chondritic portion of the Adzhi-Bogdo breccia, REE in apatite show the
336 characteristic smooth slope from La to Lu and no or only a minor Eu anomaly (Fig. 6d). However,
337 those in the differentiated clasts (achondritic fragments) have flat REE patterns (La/Lu ≈ 0.94-1.34)
338 and a prominent negative Eu anomaly (Eu/Eu* ≈ 0.21), similar to apatites from differentiated
339 meteorites (Fig. 7).

340 Apatite from achondrites has significantly higher REE contents and shows slightly
341 fractionated to flat REE-patterns with a pronounced negative Eu anomaly (Fig. 7). Apatite from the
342 acapulcoites Dhofar 125 and Acapulco (Fig. 7a), as well as from the ureilitic trachyandesite ALM-A
343 (Fig. 7b) exhibit similar enrichment of up to 300 × CI. Their REE-patterns show a smooth decline
344 from LREE to HREE (La/Lu ≈ 5.4) and a pronounced negative Eu anomaly (Eu/Eu* ≈ 0.19). The
345 pattern and enrichment of Acapulco apatite reported by Zipfel et al. (1995) are in good agreement
346 with the data obtained in this study (Fig. 7a). Apatite from the winonaite HaH 193 has a large spread
347 in overall enrichment (15-160 × CI; Fig. 7b), but is in agreement with the values reported in Floss et
348 al. (2007). The REE-patterns have a less prominent slope from LREE to HREE (La/Lu ≈ 1.99), but
349 also have well-defined negative Eu anomalies (Eu/Eu* ≈ 0.4).

Apatite in the eucrite NWA 5073 has the highest REE enrichment (up to 3,000 × CI; Fig. 7c) and its negative Eu anomaly (Eu/Eu* ≈ 0.03) extends over two orders of magnitude. The analyses are similar to REE data on eucritic apatites published by Hsu and Crozaz (1996), although the HREE appear slightly less enriched (Fig. 7c). Apatite from the eucrite Millbillillie is significantly less REE enriched then apatite from NWA 5073 (Fig. 7c), but it exhibits the same smooth decrease from La to Lu (La/Lu ≈ 2.1) and also the significant negative Eu anomaly (Eu/Eu* ≈ 0.09; Fig. 7c). Apatite from the Landes IAB iron meteorite is significantly less enriched in REE (~30 × CI) and has a flat pattern with a small negative Eu anomaly (Eu/Eu* ≈ 0.6) and a slightly positive slope, due to a slight depletion in La and enrichment in Yb and Lu (Fig. 7c).

REE in Merrillite. Meteoritic merrillite shows three main REE patterns with varying shapes and absolute abundances, as illustrated in Figures 8 and 9:

1) REE patterns of merrillite in ordinary chondrites (Fig. 8a) and acapulcoites (Fig. 8b) resemble those of achondritic apatites (Fig. 7). Ordinary chondrites (Fig. 8a) feature merrillite with flat REE-patterns showing a slight negative gradient from LREE to HREE and a prominent negative Eu anomaly (La/Lu ≈ 3.31; Eu/Eu* ≈ 0.56). The obtained data overlap with the results of Crozaz et al. (1989), but the Ybbsitz and Devgaon samples extend the lower limit of the REE-range, while Adzhi-Bogdo extends the upper limit (Fig. 8a). It is noted that the assemblage of merrillite surrounding the CAI in Devgaon (Fig. 2b) does not deviate in its REE pattern or enrichment. Merrillite in Acapulco exhibits the same basic shape of its REE-pattern, slightly depleted in the HREE (La/Lu ≈ 1.99) and a prominent negative Eu anomaly (Eu/Eu* ≈ 0.14), which is within the range of merrillite REE data provided by Zipfel et al. (1995; Fig. 8b). On the other hand merrillite from the second acapulcoite NWA 1052 analyzed deviates and shows a bow-shaped REE pattern: The negative Eu anomaly is less pronounced (Eu/Eu* ≈ 0.55), and while the LREE decrease in their

373 enrichment from La to Sm, the HREE increase in their enrichment from Gd to Lu, resulting in an
374 overall La/Lu value of ≈ 1.29 (Fig. 8b).

375 2) In some differentiated meteorites, merrillite has quite unfractionated REE-patterns without
376 prominent anomalies, e.g. the mesosiderite Dalgaranga (La/Lu ≈ 0.99-1.50; Eu/Eu* ≈ 1.1-1.5;
377 Fig. 8c). Crozaz et al. (1985) reported a similarly unfractionated pattern for merrillite from Emery
378 mesosiderite, but also two LREE-depleted patterns for merrillite in Vaca Muerta and Morristown
379 mesosiderites. The former shows a negative, the latter a positive Eu anomaly of similar magnitude
380 (Fig. 8c). Merrillite from the Bondoc mesosiderite also lacks prominent fractionation, but
381 abundances smoothly decrease from La to Lu (La/Lu ≈ 1.93) and there only is a minor negative Eu
382 anomaly (Eu/Eu* ≈ 0.6; Fig. 8c). The REE-pattern of merrillite from silicate portions of the silicate-
383 bearing Landes IAB iron meteorite is fairly flat (Fig. 8c).

384 Although REE patterns in enriched shergottites, a subgroup of the Martian meteorites, are
385 similar to mesosiderites, REE abundances are an order of magnitude higher: Northwest Africa 4864
386 (La/Lu ≈ 1.15-1.45; Eu/Eu* ≈ 0.77-1.07; Fig. 9a), Zagami (La/Lu ≈ 0.99-2.38; Eu/Eu* ≈ 0.76-1.09;
387 Fig. 9a) and KG 002 (La/Lu ≈ 1.55-2.04; Eu/Eu* ≈ 0.65-0.81; Fig. 9a).

388 3) Depleted Shergottites have a characteristic depletion in the LREE (i.a., La/Yb ≈ 0.1; Borg et al.
389 1997; McCubbin et al. 2012), and merrillites from this subgroup show this feature as well. Merrillite
390 in SaU 005 and DaG 1051 shows highly LREE-depleted patterns (La/Lu ≈ 0.17) that are in the
391 upper range of merrillite REE data reported from other depleted shergottites by Shearer et al. (2015).
392 They have a small negative Eu anomaly (Eu/Eu* ≈ 0.55; Fig. 9b). The Ca-phosphates in both
393 enriched and depleted shergottites mimic the REE pattern of their respective bulk meteorite (except
394 for Eu anomalies), but, compared to their hosts, their REE concentrations are elevated by two
395 orders of magnitude (Fig. 9).

396 **Other trace elements**. Additional Ca-phosphate trace element concentrations (Sc, Ti, V,
397 Cr, Mn, Co, As, Rb, Sr, Y, Zr, Nb, Ba, Hf, Ta, Pb, Th and U, obtained by LA-ICP-MS) are available
398 within the supplemental material (supplemental Table S1). Their abundances in both species are
399 variable from meteorite to meteorite (Figs. 10 and 11). In all investigated samples Ti, V, Cr, Mn, and
400 Co always show subchondritic concentrations, while Sr, Y, Th and U are always enriched relative to
401 CI in both phosphates. Arsenic, Rb, Zr, Nb, Ba, Hf, Ta, and Pb abundances vary from sub- to
402 superchondritic (Figs. 10 and 11). In contrast to REE and Y, the abundances of the remaining trace
403 elements (listed above) in merrillite do not generally exceed those of apatite.

404 Both phosphate species incorporate U and Th, yet for most samples their concentrations are
405 higher in apatite, except for the ordinary chondrite Devgaon (H3.8), in which the U- and Th
406 concentrations of merrillite exceed those of apatite. The same holds for the eucrite Millbillillie, in
407 which apatite does exceed merrillite in U but not in Th content (Table S1). In apatite, both U and Th
408 are positively correlated and their concentrations increase both with their host rock's grade of
409 metamorphism (petrologic type), as well as with increasing differentiation of their respective parent
410 body (Fig. 12): Apatite from Devgaon (H3.8) and Ybbsitz (H4) has the lowest concentrations of
411 <0.5 ppm U and <0.3 ppm Th, while apatite from Bruderheim (L6), Villalbeto de la Peña (L6),
412 Portales Valley (H6) and in the petrologic type 6 fragments of Adzhi-Bogdo (LL3-6), has
413 concentrations of 2.1-5.5 ppm U and 2.3-8.3 ppm Th (Table S1). Achondritic apatite has even higher
414 concentrations (Fig. 12), starting with primitive achondrites at 3.1-10.7 ppm U and 4.85-17.4 ppm Th
415 in acapulcoites, followed by Martian meteorites with 4.8-5 ppm U and 17.1-21.0 ppm Th in
416 shergottites (Table S1, Fig. 12). Eucritic apatite has the highest abundances obtained in this study,
417 with 35.8-164.3 ppm U and 22.4-104.9 ppm Th (Table S1), although Millbillillie apatite has a lower
418 Th/U value (Fig. 12). The range of U and Th concentrations in apatite from lunar samples (Nemchin

et al. 2009) as well as from terrestrial lherzolites (O'Reilly and Griffin 2000) exceed those of apatite from the HED-suite (Fig. 12).

Otherwise, there are no universal systematic differences among differentiated samples and chondrites and we observed no resolvable trends in the remaining trace element inventory correlating with the petrologic type of their host rocks in chondritic Ca-phosphates.

Apatite from Bruderheim (L6) shows exceptionally high concentrations for V, Rb, Sr, Zr, Nb, Ba, Hf, and Ta exceeding those of apatite from other chondrites by at least one order of magnitude (Fig. 10a). Ca-phosphate species in Ybbsitz (H4) stand out due to their high Pb concentrations in both apatite (200-1800 ppm) and merrillite (450-2200 ppm) (Fig. 10a, Tab. S1).

Although the Adzhi-Bogdo (LL3-6) polymict breccia is a fall (Tab. 1), some phosphate analyses contain relatively high concentrations of Ba and/or Sr. Both phosphate species in the exotic differentiated (granite-like) clasts show higher abundances of Zr, Nb, Hf, Ta and Pb compared to their counterparts in the chondritic portion.

Merrillite in Devgaon has unusually high Ti, V, Cr and Mn content (Fig. 10b) and furthermore, its assemblage surrounding a CAI (Fig. 2b) has higher concentrations of the refractory elements Sc, Ti, and V, as well as of the more volatile elements Cr and Mn when compared with merrillite within the remaining sample. However, the REE pattern of the CAI-associated merrillite does not diverge from the remaining merrillite in Devgaon. Although its overall enrichment is in the upper range of all merrillite within this sample, some merrillites from silicate assemblages have indistinguishable enrichments (supplemental table S1).

The trace element inventory of phosphates from differentiated meteorites does not differ strikingly from that of chondrites (Fig. 11). Yttrium consistently has the highest abundances of the additional trace elements reaching contents of ~1.8 wt% in the Millbillillie eucrite accompanied by high concentrations of Zr (~1800 ppm) and Hf (up to ~2000 ppm). Apatite from the other eucrite

(NWA 5073) also has high Y- (~2300 ppm) and Zr- (~450 ppm) abundances (Fig. 11c). High abundances of Y and REE in eucritic merrillite (compare Fig. S3) were also observed by Delaney et al. (1984b), which are only exceeded in lunar merrillite (Jolliff et al. 2006).

Although Ca-phosphates in enriched and depleted shergottites can clearly be distinguished from each other in terms of their REE abundances, there are no prominent differences among most of the remaining trace element concentrations (Fig. 11d), except for merrillite in depleted shergottites, which shows lower Pb (~0.21 vs. ~1.6 × CI) and Th (~37 vs. ~525 × CI), but higher Cr (~0.01 vs. ~0.0006 × CI) abundances than those in the enriched subgroup. Merrillite from both mesosiderites Bondoc and Dalgaranga has high abundances of Co (up to 1400 ppm) and Cr (up to 190 ppm), as well as moderately high Mn (up to 1900 ppm) concentrations (Fig. 11b).

Discussion

General observations on compositional variations in meteoritic Ca-phosphates.

Both phosphate species are the major hosts for REE in many investigated samples and, hence, usually incorporate a large fraction of their host rock's bulk REE budget, consistent with results of e.g., Ebihara and Honda (1983). However, this does not apply for all samples from our suite, as discussed later.

The high partition coefficients and consequently high suitability of REEs for incorporation into the crystal structures of merrillite and apatite results in Ca-phosphate REE concentrations up to two orders of magnitude higher than the bulk concentrations of their hosts (Figs. 8-9). Within the different samples, both merrillite and apatite show variations in their REE enrichments. However, the particular shape of their REE-patterns remains similar, suggesting that the phosphates within each sample formed under similar conditions. Matching observations of the REE patterns have been reported by e.g., Delaney (1982), Ebihara and Honda (1983), Crozaz and Zinner (1985), Davis et al.

466 (1993), Hsu and Crozaz (1996), or Shearer et al. (2015). Despite this uniformity within single
467 samples, REE-patterns are not unique for distinct meteorite groups and members therein; instead,
468 characteristic REE-patterns recur throughout the extraterrestrial suite of samples. These patterns do
469 not seem to correlate to specific adjacent mineral assemblages (e.g. metal vs. silicate dominated), nor
470 to the grade of metamorphism (petrologic type), or distinct grain-size intervals. Nevertheless, the
471 presence of plagioclase in a given phosphate paragenesis influences the magnitude of negative Eu
472 anomalies as Eu^{2+} is preferentially incorporated into plagioclase, and therefore allows to infer a
473 crystallization sequence of these phases.

474 Furthermore, different groups exhibit variations with regards to their overall Ca-phosphate
475 REE concentrations, as both species from differentiated samples show higher REE contents than
476 those of chondrites. Within the differentiated meteorites, Ca-phosphates of eucrites show
477 significantly higher REE concentrations than e.g. those from mesosiderites (Fig. 8). In general, the
478 overall REE enrichment of the Ca-phosphates is strongly influenced by their formation mechanism
479 and environment (igneous processes vs. metamorphism/metasomatism). For example, high
480 phosphate/melt partition coefficients result in enormous REE concentrations in eucrites and lunar
481 rocks (Delaney et al. 1984b, Jolliff et al. 1993, 2006). However, the overall REE enrichment does not
482 appear to be universally diagnostic, as high REE abundances are not present in all Ca-phosphates
483 that have formed in a magmatic environment. For instance, Ca-phosphates from igneous
484 assemblages in the ureilitic trachyandesite ALM-A (Fig. 7) and those from shergottites (Fig. 9) exhibit
485 significantly lower REE contents than eucritic phosphates (Figs. 7 and 8). In addition, the source
486 melt composition strongly influences the degree of REE enrichment in both phosphate species. Ca-
487 phosphates in shergottites and eucrites both crystallized in a magmatic environment, but Mars is
488 significantly less volatile depleted than the HED parent body (Dreibus & Wänke 1985). Hence the
489 lower phosphorus content - a moderately volatile element - in eucrites entails significantly lower

490 modal abundances of Ca-phosphates. Therefore, the available REE, which are favorably
491 incorporated in late crystallizing apatite and merrillite, are concentrated in the few crystallizing Ca-
492 phosphates and therefore reach the higher abundances observed in both species from eucrites
493 compared to Martian shergottites.

494 **Phosphate characteristics in chondrites**

495 Despite modifications inflicted by shock and thermal metamorphism or aqueous alteration,
496 chondrites represent the oldest and, much more importantly, very primitive extraterrestrial material
497 that has not been processed by differentiation on a global/parent-body scale. Ca-phosphates are
498 typical accessory phases in all groups of the ordinary chondrites but are less common in
499 carbonaceous chondrites (Van Schmus and Ribbe 1969; Brearley and Jones 1998). Moreover, they
500 occur in associations with all major chondrite constituents. Although they have been observed in
501 primitive (type 3) samples (e.g., Rubin and Grossman 1985; Murty et al. 2004), they are more
502 common and larger in chondrites of higher petrologic types. The initial process of Ca-phosphate
503 formation in chondrites is the oxidation of P originally dissolved in alloys of Ni,Fe-metal (Göpel et
504 al. 1994). In general, this takes place at relatively low temperatures, reliant on the quantity of available
505 P in the Fe,Ni-metal, as well as on the oxygen fugacity present during the formation process (Olsen
506 and Fuchs 1967; Zipfel et al. 1995). During the subsolidus reaction CaO and the remaining
507 constituents are provided by adjacent silicates and matrix, predominantly pyroxene (but also olivine
508 and plagioclase), enabling the formation of phosphates, which also inherit their trace elements from
509 the surrounding silicates during metamorphic redistribution (Zipfel et al. 1995). Jones et al. (2014,
510 2016) correlate this process primarily with the formation of merrillite, as the apatite X-site
511 composition (c.f. Fig. 5) does not equilibrate with increasing petrologic type. Therefore, they suggest
512 that chondritic phosphates either have been formed by precipitation from a very dry, P- and S-

513 bearing, halogen-rich fluid, or by metasomatic reactions with major silicate phases and/or (in the
514 case of apatite) preexisting metamorphic merrillite.

515 Most chondrites commonly feature both Ca-phosphates, yet the Allegan H5 chondrite
516 contains only merrillite. Possibly, the necessary volatiles to form apatite (ordinary chondrites are
517 dominated by Cl-apatite, cf. Fig. 5) were not available in sufficient quantity during their formation.

518 Despite the variety of chondritic groups, both Ca-phosphate species maintain a remarkably
519 constant chemical composition (Fig. 4; Table 3): Apatite from ordinary chondrites varies by only 0.17
520 wt% in its MgO content (b.d.-0.17 wt%), and by 0.25 wt% in its Na_2O concentration (~0.25-0.5
521 wt%). However, FeO variations are scattered and exceed 2 wt% (Fig. 4). For Karoonda (CK4), the
522 high FeO range might be caused by a partial overlap with small magnetite inclusions within some
523 apatite grains (Fig. 2c). Merrillite in ordinary chondrites exhibits slightly larger variations, as Na, Mg
524 (and Fe) are among its structural components. Apatite in ordinary chondrites shows a limited range
525 of REE enrichment (up to 125 × CI), smoothly decreasing from La to Lu. Europium shows the only
526 deviations, either exhibiting positive anomalies in Devgaon and Portales Valley, or slightly negative
527 anomalies in Bruderheim, Villalbeto de la Peña, Adzhi-Bogdo and Ybbsitz, the latter congruent with
528 previously reported data (Fig. 6). The largest influence on the orientation and intensity of a Eu
529 anomaly is the formation of plagioclase: Eu (in divalent state at reducing conditions) favors the
530 plagioclase crystal structure over phosphates. Therefore, if plagioclase has formed prior to the
531 phosphates, or is present in high proportion in the vicinity of phosphate formation, a negative Eu
532 anomaly is likely to form within the phosphates. Phosphates that do not have to compete
533 significantly with plagioclase, exhibit a positive Eu anomaly. However, there is no resolvable
534 diagnostic correlation between the plagioclase modal abundances or number of plagioclase grains in
535 contact with the apatite grains and the type of the Eu anomaly (positive or negative). Merrillite
536 patterns are, except for their overall REE enrichment, even less variable (Fig. 6). Their higher

537 enrichment compared to that of coexisting apatite, as well as the smooth drop of their REE patterns
538 from La to Lu, paired with the prominent negative Eu anomaly, appear to be strictly controlled by
539 the partitioning coefficients, except for Eu. This leaves the overall enrichments, as well as the
540 orientation and intensity of the Eu anomaly as the only remaining variables of merrillite REE
541 patterns. Enrichment in the LREE might also be induced by terrestrial contaminants during
542 weathering in hot deserts (Crozaz et al. 2003), which raises a possible concern for all NWA samples
543 (Table 1). However, the weathering degree of the host meteorites and their discovery as falls or finds
544 (Table 1), shows no systematic correlation with neither the LREE enrichment and La/Lu value of
545 the phosphates (Table 3 and Fig. 6), or their Ba and Sr abundances, indicative for terrestrial alteration
546 (Stelzner et al. 1999).

547 Although merrillite from the unique assemblage surrounding a CAI in Devgaon (H3.8) does
548 not show anomalies in its REE patterns, the elevated concentrations of Sc, Ti, V, Cr and Mn indicate
549 that its composition is locally controlled by (a) the refractory character of the inclusion (Sc, Ti, V)
550 and (b) its high abundance of secondarily altered spinel (Cr, Mn).

551 The only significant variations in REE abundances among chondritic Ca-phosphates are
552 documented by the REE-concentrations obtained from phosphates of the exotic clasts in the Adzhi-
553 Bogdo LL3-6 regolith breccia (Figs. 3c-d and 6d). The enrichment and REE patterns of their apatite
554 grains is not found in any typical chondrite or chondritic fragment and the patterns resemble those
555 shown by achondritic apatite (Fig. 7). In general, the same holds also for merrillite (Fig. 8). Several
556 EDX and EPMA analyses and mappings rule out an accidental measurement of apatite-merrillite-
557 intergrowth. The question remains, whether these achondritic fragments represent remnants of an
558 achondritic projectile that may have hit the Adzhi-Bogdo parent body or if they originated on the LL
559 chondrite parent body. Oxygen isotopic investigations indicate a close relationship of these clasts to
560 ordinary chondrites (Sokol et al. 2007b). However, it may be possible that a differentiated parent

body existed in the neighborhood of the LL chondrites within a very similar oxygen isotope environment, reconciling the close relationship in oxygen isotopes with the differentiated nature of these fragments.

Elevated concentration of Pb in both apatite and merrillite of ~one to two orders of magnitude are observed in Ybbsitz (H4), when compared to other ordinary chondrites (Fig. 10a, Tab. S1). This could indicate an unusual natural enrichment of radiogenic Pb (its isotope composition is not known) or common Pb contamination. It is noted that Ybbsitz shows evidence for only minor terrestrial weathering (~W1 stage; Table 1) and other trace element concentrations (i.e., REEs in Fig.6) are within the same range or even have lower abundances when compared to other ordinary chondrites. We therefore interpret this unusual enrichment of highly mobile Pb as likely terrestrial contamination of this particular sample.

Phosphate characteristics in differentiated meteorites

Acapulcoites: This group documents the processing from primitive material (their bulk composition is more or less chondritic) to evolved (differentiated) parent bodies (Mittlefehldt 2007). General mineralogy and modal compositions resemble those of chondritic samples, but chondrules are absent or just occur as relicts, and, furthermore, mineral compositions deviate from the chondritic predecessors (Mittlefehldt 2007). Both species of Ca-phosphates occur in acapulcoites, but not necessarily within the same samples. While the Acapulco meteorite contains both Ca-phosphates with an apatite/merrillite ratio of 2:1, apatite is the only species observed in Dhofar 125 (also reported by Greshake et al. 2001), and merrillite in NWA 1052, respectively (Table 1). As illustrated in Fig. 4, merrillite exhibits constant composition regarding its MgO, FeO, and Na_2O content, which covers the same compositional range occupied by chondritic merrillite. However, apatite from acapulcoites generally shows higher MgO, but lower Na_2O concentrations than in chondrites (Fig. 4). When comparing apatite within the group, Dhofar 125 shows slightly elevated

585 FeO contents (Fig. 4). Nevertheless, this might, despite its low weathering degree, be due to
586 terrestrial contamination, since it is a meteorite find (Table 1). On the other hand, Crozaz et al.
587 (2003) reported little indication for terrestrial alteration of Dhofar 125.
588 Acapulcoites feature Ca-phosphates that were most likely generated during metamorphic reactions.
589 However, Zipfel et al. (1995) have demonstrated that this does not account for the entire fraction of
590 phosphates in Acapulco, since the LREE distribution between silicates and phosphates are not
591 equilibrated; the authors instead suggested a volatile-rich, metasomatic melt as possible explanation
592 for the phosphate generation and REE inventory. Regarding their apatite REE inventory,
593 acapulcoites show a large range of REE enrichment, but nevertheless a constant relative depletion in
594 the HREE, despite variations in the LREE/HREE ratios from sample to sample (Fig. 7a). Merrillite
595 REE patterns from Acapulco are identical to those of its apatite but are slightly more enriched.
596 Merrillite from NWA 1052 represents the only Ca-phosphate species observed in this sample and
597 exhibits low REE abundances, as well as a quite different bow-shaped REE pattern with a less
598 pronounced negative Eu anomaly when compared to other acapulcoite merrillite grains (Fig. 8). This
599 divergence may be explained by the genetic relation of this sample. Despite the first classification of
600 NWA 1052 as an acapulcoite published in Russell et al. (2005), Eugster and Lorenzetti (2005) argued
601 that NWA 1058 (most likely paired with NWA 1052) is rather associated with the winonaite group,
602 based on oxygen isotopes, cosmic-ray exposure ages, and bulk chemistry. Hence, Greenwood et al.
603 (2012) list NWA 1052 among the winonaites as well, and therefore a genetic relation to the
604 winonaites may explain the uncommon bow-shaped REE patterns, which might have been inherited
605 from pyroxenes during metamorphic redistribution, since similar patterns have been reported for
606 clinopyroxene in winonaites by Floss et al. (2008).
607 **Winonaites:** On the broad scale, winonaites generally have chondritic mineralogy and
608 compositions, but have undergone extensive thermal metamorphism (Mittlefehldt, 2007; Floss et al.

609 2008). Furthermore, oxygen isotopic data possibly links the parent bodies of winonaites and IAB
610 iron meteorites (Clayton and Mayeda, 1996; Benedix et al. 2000; Floss, 2007). Although merrillite has
611 been documented in the winonaite NWA 1463, apatite appears to be winonaites' dominating Ca-
612 phosphate (Floss et al. 2008). This is supported by our study of HaH 193, where only apatite was
613 found in the analyzed section. Note that Floss et al. (2008) as well as Prinz et al. (1980) have reported
614 significant variations in the modal abundance of apatite concerning studies of different sections of
615 the same meteorite, as well as between different members of the winonaite group. The
616 inhomogeneous distribution of phosphates within different samples is likely responsible for a range
617 of different bulk REE patterns reported for winonaite samples so far (Floss et al. 2008). A large
618 spread in REE patterns is not only reflected in the bulk rock signatures, but also observed in
619 individual apatite grains within a single section of HaH 193 (Fig. 7b). This may point towards
620 different growth episodes of apatite grains, and/or to local compositional heterogeneity within
621 HaH 193 resulting in different microenvironments for Ca-phosphate formation. The general shape
622 of the REE patterns are closely associated with those obtained from acapulcoites, but the average
623 enrichment is lower (Figs. 6a-b). The bulk rock REE pattern of HaH 193 calculated by Floss et al.
624 (2007) exhibits chondritic or slightly subchondritic enrichments and is strongly dependent on apatite
625 modal abundances in the given sample, which we further discuss below. Concerning the overall REE
626 budget, apatite remains the main carrier for REEs in HaH 193, with its CI normalized enrichment
627 exceeding the calculated bulk patterns (Floss et al. 2008) by two orders of magnitude. Its
628 orthopyroxene has HREE-enriched patterns, inversely-shaped in contrast to the slightly LREE
629 enriched patterns of clinopyroxene and apatite (Floss et al. 2007). Plagioclase shows large positive Eu
630 anomalies (two orders of magnitude; Floss et al. 2007), partially balancing the negative anomalies
631 shown by the former phases.

Note that merrillite from NWA 1052 might rather indicate that this sample is associated with the winonaites instead of acapulcoites (c.f. previous paragraph). Its low REE abundances overlap with apatite from HaH 193, consistent with a comparable, metamorphic formation environment. Yet the negative Eu anomaly is less pronounced and the HREE enrichment entails a bow-shaped REE pattern. Similar patterns occur in clinopyroxene from winonaites (Floss et al., 2008), which might have handed down their REE signatures to the merrillite.

HED-meteorites: Both phosphate species occur in the HED-suite, but while they occur in numerous eucrites, they are absent in most diogenites as a consequence of their low bulk rock phosphorus abundances (Delaney et al. 1984b). Ca-phosphates also occur in howardites (Yagi et al. 1978), which are breccias consisting of eucritic and diogenitic components. Despite widespread impact-related and thermal-metamorphic modifications (e.g., Hsu and Crozaz 1996; Mittlefehldt 2007), the majority of the eucritic Ca-phosphates are clearly of igneous origin (Delaney et al. 1984a, 1984b). They are heterogeneously distributed within the eucrites (Hsu and Crozaz 1996) and are typically located in interstitial assemblages together with Ca-rich pyroxenes, ilmenite, and troilite, implying a late crystallization from local, residual melts. Delaney et al. (1984b) inferred crystallization temperatures close to the solidus, slightly below 1000°C, at the point when the bulk composition of the remaining melt had become silicic. The late crystallization from residual melts also explains the heterogeneous distribution as well as variations in apatite-merrillite proportions (Hsu and Crozaz 1996), observed throughout the eucrites. These variations are likely related to properties of the residual melts (Delaney et al. 1984b). Eucritic apatites are almost exclusively F-apatites (Fig. 5) and merrillite does not include either F or Cl (Jolliff et al. 2006). Hence, the concentration of F in the melt will have a strong effect on the apatite/merrillite ratio, as higher F contents in the melt will result in higher apatite abundances (Sarafian et al. 2017). The presence of Sc-Group (IIIA) elements possibly triggered merrillite crystallization from the interstitial melts (Delaney et al. 1984b) and

656 variations of major elements (Ca, Na, Mg, Fe, P) between the interstitial residual melts will certainly
657 have had an impact on the crystallization. Both Ca-phosphates in eucrites exhibit the lowest Na_2O
658 contents (Table S1) but the highest REE abundances (up to 30,000 × CI; Delaney et al. 1984a,
659 1984b), which are only exceeded by lunar samples (e.g. Jolliff et al. 2006). Nevertheless, the REE
660 enrichment of apatite in the Stannern-trend eucrite NWA 5073 exceeds that of apatite from the
661 Millbillillie main group eucrite by almost an order of magnitude. High REE enrichments in the NWA
662 5073 apatites are consistent with data from Hsu and Crozaz (1996) – although especially the HREE
663 are slightly less enriched – as well as the host rocks bulk composition, as it belongs to the rare group
664 of the so-called Stannern-trend eucrites characterized by high abundances in Ti and incompatible
665 elements (Hsu and Crozaz 1996; Roszjar et al., 2011). In Millbillillie, apatite has smaller grain sizes
666 (~10-15 μm vs. up to 65 μm in NWA 5073) and lower REE abundances than in NWA 5073
667 (Table 3), but the REE pattern (smooth decreasing concentration with increasing ionic radii) is still
668 present and other trace elements do not exhibit unusual concentrations. Therefore, the low REE
669 enrichment might be attributed to local dilution effects or a metamorphic formation (Crozaz et al.
670 1985). Nevertheless, the high REE abundances and textural context of merrillite from Millbillillie
671 clearly corresponds to an igneous formation process, although some intergrown assemblages of
672 apatite and merrillite in NWA 5073 may indicate a metasomatic overprint, as discussed by Roszjar et
673 al. (2011).

674 Despite the very low modal abundance of Ca-phosphates in eucrites (<0.1 vol%; Table 1),
675 Hsu and Crozaz (1996) estimated over 80% of the eucrite REE budget to be located in both species
676 combined. Additionally, zircon also incorporates significant amounts of (H- and M-)REEs and is
677 present in both analyzed eucrites (Roszjar et al. 2011, 2014), where it is located within the late-stage
678 mesostasis areas together with Ca-phosphates. Therefore, Ca-phosphates in eucrites lacking adjacent
679 zircon may reach even higher REE abundances. Interestingly, Th of Millbillillie Ca-phosphates

680 appears to favor merrillite over apatite (Table S1) which results in lower U/Th values than in NWA
681 5073 (Fig. 12).

682 The observed extreme REE-enrichment in the Millbillillie merrillites require charge balances
683 and result in lower Ca contents (Table 2b), as well as vacancies in the Na-lattice position, which has
684 also been documented by Jolliff et al. (2006) and Shearer et al. (2015). The negative correlation of Na
685 vs. Y+REE apfu is illustrated in supplemental Figure S3, however although merrillite from
686 Millbillillie plots between lunar and martian ranges, the distinct negative slope present in lunar
687 merrillite (Jolliff et al. 2006) is not pronounced within the individual samples from this study
688 (Fig. S3). In eucrites, both phosphate species exhibit a similar shape of REE patterns with a smooth
689 decrease from La to Lu and a very prominent Eu anomaly, skipping an entire order of magnitude
690 (Fig. 7). The REE patterns of pyroxene and plagioclase from numerous eucrites have been reported
691 by Hsu and Crozaz (1996), which show complementary pattern features compared to those of the
692 Ca-phosphates: plagioclase shows very prominent positive Eu anomalies, also covering two orders of
693 magnitude and pyroxene REE patterns smoothly increase from La to Lu. Since plagioclase occurs
694 early in the eucritic crystallization sequence (Stolper 1977; Hsu and Crozaz, 1996), it consumes the
695 majority of the available Eu, incorporating most divalent Eu ions. The HREE are better suited for
696 the pyroxene crystal structure, generating the slope of their pattern as a function of their ionic radii.
697 The phosphates are formed late in the crystallization sequence and have consumed the remaining
698 REE during their crystallization in the interstitial pockets of highly evolved, REE enriched melt. The
699 large spread of varying REE enrichment of phosphates within the same sample, or also within
700 different sections of the same meteorite is most likely attributed to variation in the composition of
701 the residual interstitial melt pockets, as well as their competition and timing within the crystallization
702 sequence along with other REE consuming phases.

703 **Martian meteorites:** The shergottites are basaltic meteorites originated in the shallow
704 subsurface, and their parental melts are assumed to have their origin in partial melting of the Martian
705 mantle (e.g., Borg et al. 1997, McCubbin et al. 2012). They can be divided into different subtypes
706 (enriched, intermediate, and depleted) based on their La/Yb and $^{87}Sr/^{86}Sr$ and εNd values (Borg et al.
707 1997; Kruijer et al. 2016). While the enriched subtype is assumed to have originated by varying
708 degrees of mixing or assimilation of an enriched mantle or crustal source, the depleted subtype is
709 interpreted to correspond to a mantle source region spared from substantial alteration (McCubbin et
710 al. 2012). The differences in major and minor element geochemistry between the enriched and
711 depleted shergottites are attributed to their different source regions and different proportions of
712 crustal assimilation, hence, to their different basaltic parental melts, which in turn exhibit further
713 local variations (Shearer et al. 2015, Borg et al. 1997). Shergottites generally feature both Ca-
714 phosphates, but merrillite is far more common (Tab. 2). Within the analyzed samples, all shergottites
715 feature merrillite, but apatite was only observed in the enriched subtype. Since the shergottites have
716 originated from basaltic melts (Wadhwa et al. 1994), the low phosphorous saturation (bulk
717 shergottites from this study do not exceed 1.5 wt% P; cf. Table 1), initially prevented the
718 crystallization of Ca-phosphates (Watson 1979; Green and Watson 1982) until it evolved and
719 fractionated. Therefore, the Ca-phosphates in shergottites are formed very late in the crystallization
720 sequence and are usually located in interstitial assemblages, residual melt pockets, or in symplectitic
721 associations (Figs. 2e-f). Apatite X-site composition extends over a large range (Fig. 5d) and might be
722 modified by shock events and hence does present itself as a diagnostic tool. The order of
723 crystallization concerning apatite and merrillite differs from sample to sample. Textural evidence was
724 presented by Warren et al. (2004), Gross et al. (2013), McCubbin et al. (2014), and Shearer et al.
725 (2015) for both cases. For the analyzed enriched shergottites Zagami and NWA 4864, textural
726 association of micrometer-sized apatite rims along merrillite grains (Fig. 3e), as well as large merrillite

727 grains (of several 100 μm) and a residual SiO_2-rich melt pocket cornering significantly smaller apatite
728 grains (~25-50 μm) indicate that merrillite crystallized prior to apatite.

729 The ranges of merrillite Na, Fe and Mg abundances from shergottitic samples are consistent with
730 findings from Shearer et al. (2015). The significantly lower Mg and higher Fe content of merrillite
731 from enriched shergottites (Figs. 2a and c) most likely corresponds to varying degrees of mixing and
732 crustal assimilation during the evolution of the enriched parental melt. However, both subtypes
733 (enriched and depleted) show significantly lower Na concentration when compared to other
734 meteorite groups, as illustrated in Figure 4. Merrillite mimics the bulk rock REE pattern (but is
735 enriched by two orders of magnitude), except for Eu, which is favorably incorporated in plagioclase,
736 hence creating a negative Eu anomaly in the phosphate (Fig. 9). Therefore, in shergottites, the
737 diagnostic shape of phosphate REE patterns is dictated by their parental melts.

738 **Mesosiderites:** Although both Ca-phosphate species have been reported in mesosiderites,
739 merrillite is the dominant species (Delaney et al. 1984b) and the only one observed in this study.
740 Merrillite from Dalgaranga stands out due to lower Na_2O, but higher FeO concentrations when
741 compared to merrillite from other meteorite groups. Merrillite from Bondoc also exhibits a lower
742 Na_2O content, but does not show a large range in FeO concentration (Fig. 4). The low Na_2O
743 abundances in mesosiderite merrillite appear characteristic, but unlike merrillite from the HED suite,
744 may not be a function of charge balances due to their REE budget, but are rather attributed to the
745 low bulk Na inventory of the mesosiderites as illustrated in the supplement (Fig. S2). Hence, the
746 slope of the trend shown by Jolliff et al. (2006) and Shearer et al. (2015) might be even steeper than
747 expected.

748 The unusually large range in FeO may have originated either in the bulk Dalgaranga meteorite,
749 or is a consequence of terrestrial alteration. Both mesosiderites are finds and show evidence of
750 weathering (stage W3; Table 1). However, the alignment of either phosphate species from

751 mesosiderites with those of other meteorite groups based on overlap in Na_2O and FeO vs. MgO
752 characteristics (Fig. 4), is not reflected by either the shape or enrichment of their REE profiles (Fig.
753 8c). Merrillite grains from mesosiderites show REE enrichments of 70-200 × CI, which is rather
754 modest compared to those of other achondrites (Figs. 8 and 9) and a similar range to those of
755 ordinary chondrites (Fig. 8a). However, they lack the prominent negative Eu anomaly of ordinary
756 chondrites, although Bondoc merrillite does have a small negative Eu anomaly (Fig. 8c).
757 Nevertheless, extraordinarily high positive Eu anomalies occur in pigeonite-plagioclase-clasts within
758 mesosiderites, which so far exceed those of other extraterrestrial materials (Mittlefehldt et al. 1992).
759 The modest REE abundances of Ca-phosphates from mesosiderites are probably a result of
760 enormous metal-over-silicate enrichment, followed by phosphorus partitioning out of that metal
761 (and associated phosphide) and into the silicate fraction matter as a consequence of only moderate
762 oxygen fugacity (e.g. Delaney et al. 1980; Harlow et al. 1982).

763 The Dalgaranga merrillite REE patterns basically mimic the pattern of the bulk silicate portion
764 presented by Hidaka and Yoneda (2011), but it is enriched by two orders of magnitude and lacks the
765 slight positive anomalies in La and Lu (Fig. 8c). On the bulk rock scale, Gast and McConnell (1972)
766 and Wasson (1974) suggested moderate to extensive partial melting of a source with chondritic REE
767 distributions that would generate these flat REE patterns, which are also observable in many bulk
768 howardites and eucrites, as well as in lunar samples.

769 Merrillite likely originates from subsequent metamorphic redox reactions of the silicate portion
770 and metal (Harlow et al. 1982; Crozaz et al. 1985), adopting the flat REE pattern, but incorporating
771 the majority of the available REE budget. Different orientations of Eu anomalies (positive or
772 negative, yet consistent within a given sample) or variations in the enrichment of the LREE, as seen
773 in Bondoc or reported from merrillite within other mesosiderites (Crozaz et al. 1985) are probably a
774 function of mineral proportions in the silicate fraction contributing to the REE during Ca-phosphate

775 formation. For example, merrillite showing LREE depletion coupled with a positive Eu anomaly
776 reported in the Morristown mesosiderite by Crozaz et al. (1985) was interpreted as a consequence of
777 the orthopyroxene-dominated host, from which the merrillite crystallized.

778 **IAB iron meteorites:** Trace amounts of phosphates are described in numerous IAB iron
779 meteorites (Benedix et al. 2000), and although many different and complex phosphate minerals are
780 reported in iron meteorites in general (c.f. Olsen et al. 1999), Cl-apatite and merrillite are the
781 dominant phosphate species, even though more exotic phosphates such as brianite [$Na_2CaMg(PO_4)_2$]
782 occasionally occur (Scott and Bild, 1974; Benedix et al. 2000). Phosphorus is not solely located in Ca-
783 phosphates but may also be present in phosphides [e.g. schreibersite: $(Fe,Ni)_3P$] and subordinately in
784 the metal phase. The section of the silicate-bearing Landes IAB iron meteorite analyzed in this study
785 contains merrillite and Cl-apatite (Table 2), and both are situated as large inclusions within the Fe,Ni-
786 metal (Fig. 1c). Landes is the only sample analyzed in this study in which apatite REE concentrations
787 slightly exceed those of merrillite (~20-50 × CI vs. ~15-25 × CI), although abundances in both are
788 low (Table 3). Both Ca-phosphate species show unfractionated LREE patterns, slightly depleted in
789 La. However, some differences are evident in the Eu and HREE abundances: (1) the minor negative
790 Eu anomaly featured in apatite is absent in merrillite and (2) the HREE enrichment from merrillite
791 slightly drops from Gd to Tm, while the apatite HREE pattern remains flat (Figs. 7c and 8c). These
792 diverging patterns occur in grains located in close proximity (~250 μm) to each other (Fig. 1c). The
793 higher apatite REE content is puzzling, since the merrillite crystal structure is more suitable for the
794 uptake of REE cations (Jolliff et al. 1993), typically resulting in higher REE concentration.
795 Therefore, the REE abundances of both phosphates appear to reflect their crystallization sequence.
796 The apatite inclusion may have formed prior to the merrillite incorporating higher portions of the
797 REE available in their vicinity, and only some Eu was partitioned into the adjacent plagioclase. Bild
798 (1977) analyzed La, Sm, Eu, Yb, and Lu from the silicate portion of Landes (among other IAB

irons), and the REE concentrations of both Ca-phosphates are enriched by an order of magnitude compared to the bulk portion, which has an almost chondritic REE concentration (0.64-2.61 × CI). Furthermore, the bulk silicate portion, as well as both Ca-phosphate species exhibit a depletion of La compared to Sm by about a factor of two. The ratios of other REE (e.g., Sm/Eu ≈ 1; Eu/Yb ≈ 1.1; Yb/Lu ≈ 1.3) reported by Bild (1977) correspond well with those observed in merrillite, but not with those shown by apatite (Tables 4 and S1). The two phosphate species are not the exclusive REE host phases within the silicate portion. This might be an effect of its equilibration under more reducing conditions than found for example in chondrites, which initially prevented the formation of Ca-phosphates by oxidization, as suggested by Luzius-Lange and Palme (1987) and Palme et al. (1991). The low REE enrichment of both phosphates, as well as their exclusive textural association with the metal phase indicates a secondary origin by subsequent oxidization of metal or phosphides after equilibration of the silicate portion.

The overlap of winonaites and IAB iron meteorites in their oxygen isotopic signatures and thus proposed genetic relationship (Clayton and Mayeda 1996; Benedix et al. 2000; Floss 2007) is however not reflected in the REE inventory of their Ca-phosphates observed here (Fig. 7). This consequently implies different formation conditions for the phosphates from both meteorite suites. The REE enrichment of apatite in the winonaite HaH 193 exceeds that of the Landes apatite by more than one order of magnitude and features a very prominent Eu anomaly absent in the Landes apatite (Figs. 7b-c). Moreover, unlike Landes, HaH 193 does not contain merrillite (Table 1), precluding a direct comparison. Nevertheless, the differences in Ca-phosphate REE signatures certainly do not rule out a common parent body for both meteorite groups, but rather point to diverging preconditions during their formation, supporting the model from Benedix et al. (2000) for a multi-stage formation scenario involving (re)heating, partial melting and melt-mixing, catastrophic disruption, metamorphism and quenching of the host parent body.

Ureilitic trachyandesite ALM-A: Apatite is the predominant Ca-phosphate in the ALM-A sample, which represents a trachyandesitic fragment of the ureilitic parent body (Bischoff et al. 2014). The assemblage of the lath-shaped apatites among pyroxenes and feldspar (Fig. 2d) was clearly produced by an igneous formation process. The unique composition of this sample with its high feldspar abundance (~70 vol%; plagioclase with ~$An_{10–55}$ and anorthoclase with ~$An_{5–12}$; Bischoff et al. 2014) determines its trachyandesitic classification and is also reflected in the isolated (chemical) position of its apatites in Fig. 4. The composition corresponds well to the experimental data by Feldstein et al. (2001) on disequilibrium partial melt compositions (51−56 wt% SiO_2, up to 4.4 wt% Na_2O) of an ordinary chondrite starting material used to reconstruct silica and Na-rich bulk content of the ALM-A sample (Bischoff et al. 2014). Apatite from ALM-A shows REE enrichments smoothly dropping from ~260 × CI for La to ~45 × CI for Lu, with a well-defined negative Eu anomaly (Figs. 7b and 13). The bulk REE pattern (Bischoff et al. 2014), as well as the REE patterns of the remaining phases in the assemblage are given in Figure 13 (their concentration is available in supplemental table S4). The calculated REE pattern (Fig. 13), derived from the average REE composition of individual phases (Table S4) and their modal abundances (Table 1 and Bischoff et al. 2014) is able to reproduce the measured bulk REE pattern within error, indicating that the entire REE budget and carriers are recorded. The prominent positive Eu anomaly paired with the high modal abundance of feldspar reconciles the negative Eu anomaly of the highly REE-enriched apatite and the slight positive Eu anomaly of the bulk rock REE pattern. Pyroxenes are slightly enriched in the HREE, and the feldspar REE enrichment also increases slightly from Dy to Lu, which partially balances the decreasing REE enrichment in apatite with their increasing ionic radii. Texture and REE patterns suggest that the apatite crystallized simultaneously with the surrounding phases, producing the euhedral apatite laths that occur in various sizes, either isolated within the feldspar, or sometimes embedded into pyroxenes (Fig. 2d).

REE mass balance calculations of achondrites

The high REE abundances in apatite and merrillite raise the question of how to quantify the proportion they claim from their host rocks bulk REE consumption. Samarium was chosen as a representative element to conduct some basic mass balance calculations, which are summarized in supplemental Table S5. The calculations are based on the evaluated modal abundances of both species, their respective Sm concentrations, and on available bulk Sm concentration of the host meteorites. Note that Ca-phosphates intergrown and/or replaced on a small spatial resolution and grains <5 μm may not be sufficiently covered, and therefore in few cases may not be taken into account adequately for the modal abundance evaluations, which is based on elemental mappings and SEM image documentation. Available literature data often list "phosphates" among given modal constituents without distinguishing between apatite and merrillite. However, since the REE concentrations in the latter often exceed the former by an order of magnitude, it is important to establish modal abundances taking both species into account, if they coexist in a given meteorite. Hence, the modal abundances turn out to be the limiting factor in quantifying the portion of the REE budget incorporated in the corresponding Ca-phosphate species. With increasing differences in REE content among both Ca-phosphate species, the effect of the accuracy of the determined modal proportions rises significantly. This culminates for instance in the eucrite Millbillillie, in which 0.01 vol% of merrillite consumes roughly 20% of the bulk REE Sm budget (Table S5). However, the available modal data is far from precise enough for a reliable discrimination at this level, and must await more sensitive future studies. Although some uncertainties must be taken into account here and only rough estimates can be made, it is observed that although the REE patterns of both species have consistent shapes within each sample, some samples vary more in REE enrichment than others. This entails strong deviations in the fraction of the consumed bulk REE budget, depending on whether the average, minimum or maximum concentration of the corresponding phosphate species

871 is taken into account (Table S5). For example, in the acapulcoite Dhofar 125 the Sm concentrations
872 of apatite (the only Ca-phosphate species in this sample; 1.1 vol %) ranges from 17.7 to 23.2 ppm
873 with an average of 19.1 ppm consume 96% of the bulk Sm budget if the average is used. However,
874 using the apatite maximum of 23.2 ppm Sm for the mass balance calculation in combination with the
875 1.1 vol% apatite modal abundance overextends the available bulk Sm budget of the sample
876 (Table S5). For Acapulco, the obtained modal abundances and Sm concentrations of both
877 phosphates account for 97 % of the available Sm. In the analyzed eucrites, the phosphates account
878 for up to 88% of the bulk Sm budget (Table S5). However, the enormous Sm enrichment, especially
879 in merrillite, requires a much better accuracy in the determination of modal abundances, which is not
880 available at this point. Variations in the reported and obtained modal abundances in shergottites
881 entail significant differences in the consumed portion of the Sm budget, starting with ~26% in SaU
882 005, ~50% in Zagami and ending with an overconsumption of the available Sm for DaG 1051 and
883 NWA 4864 (Table S5). The latter either indicates that the obtained available bulk Sm contents are
884 too low (which we consider unlikely), that the modal phosphate abundances are overestimated,
885 and/or that a heterogeneous distribution of phosphates occurs within the bulk rock. In the latter
886 case, several (thin) sections of the same sample should be taken into account to better evaluate the
887 distribution and occurrence of both phosphate species in a given sample, especially if the REE
888 concentrations are high and the species differ considerably in REE content. While the high REE
889 concentrations make Ca-phosphates major carrier phases for the majority of meteorite groups, they
890 only account for ~5% of the available Sm in the Landes IAB iron meteorite and only 2-19% (average
891 6%) in the winonaite HaH 193 (Table S5) indicating the presence of other REE-consuming phases.

892 Despite of the considerable uncertainties induced by the limited accuracy of the determination
893 of precise modal abundances (<1 vol %) and also by the range of REE abundances, the distribution
894 of REE among its various carrier phases needs to be understood in order to advance our

895 understanding of the igneous processes that have shaped the samples we are studying. We therefore
896 advise caution concerning the estimation of modal fractions and furthermore encourage
897 discrimination of the different species, instead of merging them under the label "phosphates". In
898 order to achieve more reliable mass balance calculations, the necessary accuracy of modal estimates
899 are strongly dependent on the spatial occurrence and clear identification of the present Ca-phosphate
900 species, as well as on variation in their overall REE abundances within the sample. Moreover, if a
901 sample is brecciated, the different lithologies might differ significantly from each other and should
902 therefore be treated individually during mass balance assessments. Therefore, bulk concentrations of
903 brecciated samples may be biased depending on the included lithologies and their respective
904 proportions in the material the bulk analyses were applied to.

905 # Implications

906 Previous studies of extraterrestrial Ca-phosphates have usually targeted single meteorite
907 samples or groups, while this approach addresses the phosphate characteristics of a great variety of
908 parent bodies, shaped by different conditions and processes. We present an extensive survey of
909 occurrences, phase associations, mineralogy, and trace element chemistry of apatite-group minerals
910 and merrillite in meteorites and provide a robust and comprehensive dataset of numerous trace
911 elements, most of which have not been reported in previous studies. Hence, the dataset enables cross
912 comparison of Ca-phosphate mineralogy and chemistry in different meteorite groups, as well as
913 samples therein. Furthermore, it allows discrimination between different lithologies from brecciated
914 samples, providing a more detailed view on the complex history and evolution of brecciated rocks as
915 clearly shown here for Adzhi Bogdo (stone) and its clasts.

916 Although the Ca-phosphate trace element inventory of a distinct meteorite group is not
917 universally diagnostic to specific formation scenarios or alteration processes, the presence or absence
918 of overlap in their abundances and proportions among different meteorite groups provides the basis

919 for new approaches and correlations and also raises new questions to be addressed in future work.
920 Clearly, more work is needed to fully constrain the mechanisms during Ca-phosphate formation,
921 alteration, and their role in the evolution of planetary bodies, relevant within the context of
922 chronological constraints (e.g. U-Th-Pb systematics) in particular. Nonetheless, this study provides a
923 solid foundation and extensive data set for future studies of trace elements in meteoritic apatite and
924 merrillite, and contributes to our understanding of formation and distribution of extraterrestrial Ca-
925 phosphates.

926 ## Acknowledgements

927 We thank Marian Horstmann and Herbert Palme for productive discussions and Paul Warren,
928 Bradley Jolliff and Steve Simon for their very helpful comments and suggestions during the review
929 process. Furthermore, we also thank Beate Schmitte, Lev Ilyinsky, and Kerstin Lindén for analytical
930 support, Ulla Heitmann for thin section preparation, Klaus Mezger as a cooperation partner of a
931 related sub-project on the chronology and chemistry of meteoritic zircon and phosphate grains, and
932 Celeste Brennecka for editorial support. Moreover, Xiande Xie and Rhian Jones provided very
933 helpful comments on an earlier version of this manuscript. The NordSIMS laboratory is funded by
934 Iceland and Sweden; this is NordSIMS publication 507. This work was partly supported by the
935 German Research Foundation (DFG; Project BI 344/9-2) within the Priority Program "The First 10
936 Million Years – a Planetary Materials Approach" (SPP 1385).

937 ## References Cited

938 Armstrong, J.T. (1991) Quantitative elemental analysis of individual microparticles with electron
939 beam instruments. In K.F.J. Heinrich and D.E. Newbury, Eds., Electron Probe Quantitation,
940 p. 261–315. Springer US, Boston, MA.
941 Barrat, J.A., Blichert-Toft, J., Nesbitt, R.W., and Keller, F. (2001) Bulk chemistry of Saharan
942 shergottite Dar al Gani 476. Meteoritics & Planetary Science, 36 (1), 23–29.

Barrat, J.A., Zanda, B., Moynier, F., Bollinger, C., Liorzou, C., and Bayon, G. (2012) Geochemistry of CI chondrites: Major and trace elements, and Cu and Zn isotopes. Geochimica et Cosmochimica Acta, 83, 79–92.

Bellucci, J.J., Whitehouse, M.J., John, T., Nemchin, A.A., Snape, J.F., Bland, P.A., and Benedix, G.K. (2017) Halogen and Cl isotopic systematics in Martian phosphates: Implications for the Cl cycle and surface halogen reservoirs on Mars. Earth and Planetary Science Letters, 458, 192–202.

Bendel, V. (2013) Volatilitätskontrollierte Fraktionierung refraktär-lithophiler Elemente in Meteoriten und der Erde: Dissertation zur Erlangung des mathematisch-naturwissenschaftlichen Doktorgrades der Georg-August-Universität Göttingen, 157 p. Dissertation, Georg-August-Universität, Göttingen.

Benedix, G.K., McCoy, T.J., Keil, K., and Love, S.G. (2000) A petrologic study of the IAB iron meteorites: Constraints on the formation of the IAB-winonaite parent body. Meteoritics & Planetary Science, 35 (6), 1127–1141.

Bischoff, A., and Geiger, T. (1995) Meteorites from the Sahara: Find locations, shock classification, degree of weathering and pairing. Meteoritics, 30 (1), 113–122.

Bischoff, A., Geiger T., Palme H., Spettel, B., Schultz L., Scherer P., Schlüter J., and Lkhamsuren J. (1993) Mineralogy, chemistry, and noble gas contents of Adzhi-Bogdo – an LL3-6 chondritic breccia with foreign clasts. Meteoritics, 28 (4), 570–578.

Bischoff, A., Dyl, K.A., Horstmann, M., Ziegler, K., Wimmer, K., and Young, E.D. (2013) Reclassification of Villalbeto de la Peña – occurrence of a winonaite-related fragment in a hydrothermally metamorphosed polymict L-chondritic breccia. Meteoritics & Planetary Science, 48 (4), 628–640.

Bischoff, A., Horstmann, M., Barrat, J.A., Chaussidon, M., Pack, A., Herwartz, D., Ward, D., Vollmer, C., and Decker, S. (2014) Trachyandesitic volcanism in the early solar system. Proceedings of the National Academy of Sciences of the United States of America, 111 (35), 12689–12692.

Bild, R.W. (1977) Silicate inclusions in group IAB irons and a relation to the anomalous stones Winona and Mt. Morris. Geochimica et Cosmochimica Acta, 41 (10), 1439–1456.

Borg, L.E., Nyquist, L.E., Taylor, L.A., Wiesmann, H., and Shih, C.-Y. (1997) Constraints on Martian differentiation processes from Rb-Sr and Sm-Nd isotopic analyses of the basaltic shergottite QUE 94201. Geochimica et Cosmochimica Acta, 61 (22), 4915–4931.

975 Boyce, J.W., Tomlinson, McCubbin, F.M., Treiman, A.H., and Greenwood, J.P. (2014) The lunar
976 apatite paradox. Science, 344, 400–402.
977 Brearley, A.J., and Jones, R.H. (1998) Chondritic meteorites. In: J.J. Papike (ed), Reviews in
978 Mineralogy: Planetary Materials, 36, pp. 3-1–3-398, Mineralogical Society of America,
979 Washington, D.C.
980 Bunch, T.E., Keil, K., and Huss, G.I. (1972) The Landes meteorite. Meteoritics & Planetary Science,
981 7, 31–38.
982 Clayton, R.N., and Mayeda, T.K. (1996) Oxygen isotope studies of achondrites. Geochimica et
983 Cosmochimica Acta, 60 (11), 1999–2017.
984 Crozaz, G., and Zinner, E. (1985) Ion probe determinations of the rare earth concentrations of
985 individual meteoritic phosphate grains. Earth and Planetary Science Letters, 73 (1), 41-52.
986 Crozaz, G., Zinner, E., and Delaney, J.S. (1985) Rare earth element concentrations of mesosiderite
987 merrillite. Meteoritics, 20, 629.
988 Crozaz, G., Pellas, P., Bourot-Denise, M., de Chazal, S.M., Fiéni, C., Lundberg, L.L., and Zinner, E.
989 (1989) Plutonium, uranium and rare earths in the phosphates of ordinary chondrites - the
990 quest for a chronometer. Earth and Planetary Science Letters, 93 (2), 157–169.
991 Crozaz, G., Floss, C., and Wadhwa, M. (2003) Chemical alteration and REE mobilization in
992 meteorites from hot and cold deserts. Geochimica et Cosmochimica Acta, 67 (24), 4727–4741.
993 Davis, A.M., and Olsen, E.J. (1991) Phosphates in pallasite meteorites as probes of mantle processes
994 in small planetary bodies. Nature, 353 (6345), 637–640.
995 Davis, A.M., Prinz, M., and Weisberg, M.K. (1993) Trace element distributions in primitive
996 achondrites. REE in primitive achondrites. Lunar and Planetary Science, XXIV, 375–376,
997 (abstract).
998 Delaney, J.S., Prinz, M., and Nehru, C.E. (1980) Olivine clasts from mesosiderites and howardites -
999 clues to the nature of achondritic parent bodies. Proceedings of the 11th Lunar and Planetary
1000 Science Conference, Volume 2, 1073-1087, New York, Pergamon Press.
1001 Delaney, J.S. (1982) Minor components of basaltic Achondrites - ii. Phosphorus. Lunar and
1002 Planetary Science, XIII, 150–151 (abstract).
1003 Delaney, J.S., Prinz, M., and Takeda, H. (1984a) The polymict eucrites. Journal of Geophysical
1004 Research, 89 (S01), C251.
1005 Delaney, J.S., O'Neill, C., and Prinz, M. (1984b) Phosphate minerals in eucrites. Lunar and Planetary
1006 Science, XV, 208–209 (abstract).

Dreibus, G., and Wänke, H. (1985) Mars, a volatile-rich planet. Meteoritics, 20, 367–381.

Dreibus, G., Spettel, B., Haubold, R., Jochum, K.P., Palme, H., Wolf, D., and Zipfel, J. (2000) Chemistry of a new shergottite: Sayh al Uhaymir 005. Meteoritics & Planetary Science, 35 (S5), A49.

Dyl, K.A., Bischoff, A., Ziegler, K., Young, E.D. Wimmer, K., and Bland, P.A. (2012) Early solar system hydrothermal activity in chondritic asteroids on 1-10-year timescales. Proceedings of the National Academy of Sciences of the United States of America, 109:18306-18311.

Dyl, K.A., Boyce, J.W., Guan, Y., Bland, P.A., Eiler, J.M., and Reddy, S.M. (2015) OH, F−bearing apatite, merrillite, and halogen−poor fluids in Allende (CV3). Lunar and Planetary Science, XLVI, abstract 2927.

Easton, A.J., and Elliott, C.J. (1977) Analyses of some meteorites from the British Museum (Natural History) collection. Meteoritics, 12 (4), 409–416.

Ebihara, M., and Honda, M. (1983) Rare earth abundances in chondritic phosphates and their implications for early stage chronologies. Earth and Planetary Science Letters, 63 (3), 433-445.

Eugster, O., and Lorenzetti, S. (2005) Cosmic-ray exposure ages of four acapulcoites and two differentiated achondrites and evidence for a two-layer structure of the acapulcoite/lodranite parent asteroid. Geochimica et Cosmochimica Acta, 69 (10), 2675–2685.

Fitzgerald, M.J. (1979) The chemical composition and classification of the Karoonda meteorite. Meteoritics, 14, 109–115.

Floss, C., Jolliff, B.L., Benedix, G.K., Stadermann, F.J., and Reid, J. (2007) Hammadah al Hamra 193: the first amphibole-bearing winonaite. American Mineralogist, 92 (4), 460–467.

Floss, C., Crozaz, G., Jolliff, B.L., Benedix, G.K., and Colton, S. (2008) Evolution of the winonaite parent body: Clues from silicate mineral trace element distributions. Meteoritics & Planetary Science, 43 (4), 657–674.

Folco, L., Franchi, I.A., D'Orazio, M., Rocchi, S., and Schultz, L. (2000) A new Martian meteorite from the Sahara: The shergottite Dar al Gani 489. Meteoritics & Planetary Science, 35 (4), 827–839.

Gast, P.W., and McConnell, R.K. (1972) Evidence for initial chemical layering of the Moon. Lunar and Planetary Science, III, 289–290 (abstract).

Gladney, E.S., and Roelandts, I. (1988) 1987 compilation of elemental concentration data for USGS BIR-1, DNC-1 and W-2. Geostandards and Geoanalytical Research, 12 (1), 63–118.

1038 Green, T.H., and Watson, E.B. (1982) Crystallization of apatite in natural magmas under high
1039 pressure, hydrous conditions, with particular reference to 'Orogenic' rock series. Contributions
1040 to Mineralogy and Petrology (79), 96–105.
1041 Greenwood, R.C., Franchi, I.A., Gibson, J.M., and Benedix, G.K. (2012) Oxygen isotope variation in
1042 primitive achondrites: The influence of primordial, asteroidal and terrestrial processes.
1043 Geochimica et Cosmochimica Acta, 94, 146–163.
1044 Greshake, A., Clayton, R.N., and Mayeda, T.K. (2001) Dhofar 125: A new acapulcoite from Oman.
1045 Lunar and Planetary Science, XXXII, abstract 1325.
1046 Gross, J., Filiberto, J., and Bell, A.S. (2013) Water in the Martian interior: Evidence for terrestrial
1047 MORB mantle-like volatile contents from hydroxyl-rich apatite in olivine-phyric shergottite
1048 NWA 6234. Earth and Planetary Science Letters, 369-370, 120-128.
1049 Göpel, C., Manhès, G., and Allègre, C.J. (1994) U-Pb systematics of phosphates from equilibrated
1050 ordinary chondrites. Earth and Planetary Science Letters, 121 (1-2), 153–171.
1051 Haas, J.R., and Haskin, L.A. (1991) Compositional variations among whole-rock fragments of the L6
1052 chondrite Bruderheim. Meteoritics, 26 (1), 13–26.
1053 Harlow, G.E., Delaney, J.S., Nehru, C.E., and Prinz, M. (1982) Metamorphic reactions in
1054 mesosiderites: origin of abundant phosphate and silica. Geochimica et Cosmochimica Acta, 46
1055 (3), 339–348.
1056 Herpfer, M.A., Larimer, J.W., and Goldstein, J.I. (1994) A comparison of metallographic cooling rate
1057 methods used in meteorites. Geochimica et Cosmochimica Acta, 58 (4), 1353–1365.
1058 Hidaka, H., and Yoneda, S. (2011) Neutron capture records of mesosiderites and an iron meteorite.
1059 Geochimica et Cosmochimica Acta, 75 (19), 5706–5715.
1060 Horstmann, M., and Bischoff, A. (2014) The Almahata Sitta polymict breccia and the late accretion
1061 of asteroid 2008 TC_3. Chemie der Erde - Geochemistry, 74 (2), 149–183.
1062 Hsu, W., and Crozaz, G. (1996) Mineral chemistry and the petrogenesis of eucrites: i. noncumulate
1063 eucrites. Geochimica et Cosmochimica Acta, 60 (22), 4571–4591.
1064 Hughes, J.M., Jolliff, B.L., and Rakovan, J. (2008) The crystal chemistry of whitlockite and merrillite
1065 and the dehydrogenation of whitlockite to merrillite. American Mineralogist, 93 (8-9), 1300–
1066 1305.
1067 Jarosewich, E. (1990) Chemical analyses of meteorites: A compilation of stony and iron meteorite
1068 analyses. Meteoritics, 25 (4), 323–337.

Jolliff, B.L., Haskin, L.A., Colson, R.O., and Wadhwa, M. (1993) Partitioning in REE-saturating minerals: theory, experiment, and modelling of whitlockite, apatite, and evolution of lunar residual magmas. Geochimica et Cosmochimica Acta, 57 (16), 4069–4094.

Jolliff, B.L., Hughes, J.M., Freeman, J.J., and Zeigler, R.A. (2006) Crystal chemistry of lunar merrillite and comparison to other meteoritic and planetary suites of whitlockite and merrillite. American Mineralogist, 91 (10), 1583–1595.

Jones, R.H., McCubbin, F.M., Dreeland, L., Guan, Y., Burger, P.V., and Shearer, C.K. (2014) Phosphate minerals in LL chondrites: a record of the action of fluids during metamorphism on ordinary chondrite parent bodies. Geochimica et Cosmochimica Acta, 132, 120–140.

Jones, R.H., McCubbin, F.M., and Guan, Y. (2016) Phosphate minerals in the H group of ordinary chondrites, and fluid activity recorded by apatite heterogeneity in the Zag H3-6 regolith breccia. American Mineralogist, 101, 2451-2467.

Kiesl, W., and Kluger, F. (1981) The Ybbsitz-Meteorite. Meteoritics, 16, 339.

Joy, K.H., Nemchin, A.A., Grange, M.L., Lapen, T.J., Peslier, A.H., Ross, D.K., Zolensky, M.E., and Kring, D.A. (2014) Petrography, geochronology and source terrain characteristics of lunar meteorites Dhofar 925, 961 and Sayh al Uhaymir 449. Geochimica et Cosmochimica Acta, 144, 299–325.

Kiesl, W., and Kluger, F. (1981) The Ybbsitz-Meteorite. Meteoritics, 16, 339.

Klemme, S., Prowatke, S., Münker, C., Magee, C., Lahaye, Y., Zack, T., Kasemann, S.A., Cabato, E.J.A., and Kaeser, B. (2008) Synthesis and preliminary characterisation of new silicate, phosphate and titanite reference glasses. Geostandards and Geoanalytical Research (32), 39–54.

Kruijer, T.S., Kleine, T., Borg, L., Brennecka, G.A., Fischer-Gödde, M., Irving, A.J., Bischoff, A., and Agee, C. B. (2016) Coupled ^{142}Nd-^{182}W evidence for early crust formation on Mars. Lunar and Planetary Science, XLVII, abstract 2115.

Laul, J.C., and Smith, M.R. (1986) Rare earth patterns in shergottite phosphates. Lunar and Planetary Science, XVII, 464–465 (abstract).

Lepland, A., and Whitehouse, M.J. (2011) Metamorphic alteration, mineral paragenesis and geochemical re-equilibration of early Archean quartz–amphibole–pyroxene gneiss from Akilia, Southwest Greenland. International Journal of Earth Sciences, 100 (1), 1–22.

Lewis, J.A., and Jones, R.H. (2016) Phosphate and feldspar mineralogy of equilibrated L chondrites: The record of metasomatism during metamorphism in ordinary chondrite parent bodies. Meteoritics & Planetary Science, 51 (10), 1886–1913.

Llorca, J., Roszjar, J., Cartwright, J.A., Bischoff, A., Ott, U., Pack, A., Merchel, S., Rugel, G., Fimiani, L., Ludwig, P., Casado, J.V., and Allepuz, D. (2013) The Ksar Ghilane 002 shergottite - the 100th registered Martian meteorite fragment. Meteoritics & Planetary Science, 48 (3), 493–513.

Lodders, K. (1998) A survey of shergottite, nakhlite and chassigny meteorites whole-rock compositions. Meteoritics & Planetary Science, 33 (S4), A183-A190.

Luzius-Lange, D., and Palme, H. (1987) Trace elements in single mineral grains from silicate inclusions in the Landes meteorite. Lunar and Planetary Science, XVIII, 586–587 (abstract).

McCoy, T.J., Taylor, G., and Keil, K. (1992) Zagami: Product of a two-stage magmatic history. Geochimica et Cosmochimica Acta, 56 (9), 3571–3582.

McCubbin, F.M., and Jones, R.H. (2015) Extraterrestrial apatite: Planetary geochemistry to astrobiology. Elements, 11 (3), 183–188.

McCubbin, F.M., Steele, A., Hauri, E.H., Nekvasil, H., Yamashita, S., and Hemley, R.J. (2010) Nominally hydrous magmatism on the moon. Proceedings of the National Academy of Sciences of the United States of America, 107 (25), 11223-11228.

McCubbin, F.M., Jolliff, B.L., Nekvasil, H., Carpenter, P.K., Zeigler, R.A., Steele, A., Elardo, S.M., and Lindsley, D.H. (2011) Fluorine and chlorine abundances in lunar apatite: implications for heterogeneous distributions of magmatic volatiles in the lunar interior. Geochimica et Cosmochimica Acta, 75 (17), 5073-5093.

McCubbin, F.M., Hauri, E.H., Elardo, S.M., Vander Kaaden, K. E., Wang, J., and Shearer, C.K. (2012) Hydrous melting of the Martian mantle produced both depleted and enriched shergottites. Geology, 40 (8), 683–686.

McCubbin, F.M., Shearer, C.K., Burger, P.V., Hauri, E.H., Wang, J., Elardo, S.M., and Papike, J.J. (2014) Volatile abundances of coexisting merrillite and apatite in the Martian meteorite Shergotty: implications for merrillite in hydrous magmas. American Mineralogist, 99 (7), 1347-1354.

Mikouchi, T., Miyamoto, M., and McKay, G.A. (2001) Mineralogy and petrology of the Dar al Gani 476 Martian meteorite: Implications for its cooling history and relationship to other shergottites. Meteoritics & Planetary Science, 36 (4), 531–548.

1130 Min, K., Farley, K.A., Renne, P.R., and Marti, K. (2003) Single grain (U–Th)/He ages from
1131 phosphates in Acapulco meteorite and implications for thermal history. Earth and Planetary
1132 Science Letters, 209 (3-4), 323–336.
1133 Mittlefehldt, D.W. (2007) Achondrites. In: Holland, H.D., and Turekian, K.K., Eds, Treatise on
1134 Geochemistry – Volume 1: Meteorites and Cosmochemical Processes, p. 235–266, Elsevier,
1135 Oxford.
1136 Mittlefehldt, D.W., Rubin, A.E., and Davis, A.M. (1992) Mesosiderite clasts with the most extreme
1137 positive europium anomalies among solar system rocks. Science (New York, N.Y.), 257
1138 (5073), 1096–1099.
1139 Moggi-Cecchi, V., Pratesi, G., and Mancini, L. (2005) NWA 1052 and NWA 1054: Two new
1140 primitive achondrites from North West Africa. Lunar and Planetary Science, XXXVI, abstract
1141 1808.
1142 Murty, S.V.S., Rai, V.K., Shukla, A.D., Srinivasan, G., Shukla, P.N., Suthar, K.M., Bhandari, N., and
1143 Bischoff, A. (2004) Devgaon (H3) chondrite: Classification and complex cosmic ray exposure
1144 history. Meteoritics & Planetary Science, 39 (3), 387–399.
1145 Nehru, C.E., Zucker, S.M., Harlow, G.E., and Prinz, M. (1980) Olivines and olivine coronas in
1146 mesosiderites. Geochimica et Cosmochimica Acta, 44 (8), 1103–1118.
1147 Nemchin, A.A., Pidgeon, R.T., Healy, D., Grange, M.L., Whitehouse, M.J., and Vaughan, J. (2009)
1148 The comparative behavior of apatite-zircon U-Pb systems in Apollo 14 breccias: Implications
1149 for the thermal history of the Fra Mauro Formation. Meteoritics & Planetary Science, 44 (11),
1150 1717–1734.
1151 Olsen, E., and Fuchs, L.H. (1967) The state of oxidation of some iron meteorites. Icarus, 6 (1-3),
1152 242–253.
1153 Olsen, E.J., Kracher, A., Davis, A.M., Steele, I.A., Hutcheon, I.D., and Bunch T.E. (1999) The
1154 phosphates of IIIAB iron meteorites. Meteoritics & Planetary Science, 34 (2), 285–300.
1155 O'Reilly, S.Y., and Griffin, W. (2000) Apatite in the mantle: Implications for metasomatic processes
1156 and high heat production in Phanerozoic mantle. Lithos, 53 (3-4), 217–232.
1157 Palme, H., Schultz, L., Spettel, B., Weber, H.W., Wänke, H., Michel-Levy, M.C., and Lorin, J.C.
1158 (1981) The Acapulco meteorite - chemistry, mineralogy and irradiation effects. Geochimica et
1159 Cosmochimica Acta, 45, 727–729.

Palme, H., Hutcheon, I.D., Kennedy, A.K., Sheng, Y.J., and Spettel, B. (1991) Trace Element Distribution In Minerals From A Silicate Inclusion In The Caddo IAB-Iron Meteorite. Lunar and Planetary Science, XXII, 1015–1016 (abstract).

Patiño-Douce, A.E., and Roden, M. (2006) Apatite as a probe of halogen and water fugacities in the terrestrial planets. Geochimica et Cosmochimica Acta, 70 (12), 3173–3196.

Patiño-Douce, A.E., Roden, M.F., Chaumba, J., Fleisher, C., and Yogodzinski, G. (2011) Compositional variability of terrestrial mantle apatites, thermodynamic modeling of apatite volatile contents, and the halogen and water budgets of planetary mantles. Chemical Geology, 288, 14–31.

Powell, B.N. (1971) Petrology and chemistry of mesosiderites - ii. silicate textures and compositions and metal-silicate relationships. Geochimica et Cosmochimica Acta, 35 (1), 5–34.

Prinz, M., Delaney, J.S., Harlow, G.E., Bedell, R.L., and Nehru, C.E. (1980) Modal studies of mesosiderites and related achondrites, including the new mesosiderite ALHA 77219. Proceedings of the 11th Lunar and Planetary Science Conference, Volume 2, 1055–1071, New York, Pergamon Press.

Reed, S.J.B., Smith, D.G.W., and Long, J.V.P. (1983) Rare earth elements in chondritic phosphates — implications for ^{244}Pu chronology. Nature, 306 (5939), 172–173.

Roszjar, J., Metzler, K., Bischoff, A., Barrat, J.A., Geisler, T., Greenwood, R.C., Franchi, I.A., and Klemme, S. (2011) Thermal history of Northwest Africa 5073 – a coarse-grained Stannern-trend eucrite containing cm-sized pyroxenes and large zircon grains. Meteoritics & Planetary Science, 46 (11), 1754–1773.

Roszjar, J., John, T., Whitehouse, M.J., and Layne, G.D. (2013) Halogens in the early solar system inferred from meteoritic phosphates. Mineralogical Magazine, 77 (5), 2015–2107.

Roszjar, J., Whitehouse, M.J., and Bischoff, A. (2014) Meteoritic zircon – Occurrence and chemical characteristics. Chemie der Erde - Geochemistry, 74, 453-469.

Rubin, A.E. (1997) Mineralogy of meteorite groups. Meteoritics & Planetary Science (32), 231–247.

Rubin, A.E., and Grossman, J.N. (1985) Phosphate-sulfide assemblages and Al/Ca ratios in type-3 chondrites. Meteoritics & Planetary Science, 20, 479–489.

Russell, S.S., Zolensky, M.E., Righter, K., Folco, L., Jones, R.H., Conolly, H.C., Grady, M.M., and Grossman, J.N. (2005) The Meteoritical Bulletin, no. 89, 2005 September. Meteoritics & Planetary Science, 40 (S9), A201-A263.

Ruzicka, A., Killgore, M., Mittlefehldt, D.W., and Fries, M.D. (2005) Portales Valley: Petrology of a metallic-melt meteorite breccia. Meteoritics & Planetary Science, 40 (2), 261–295.

Ruzicka, A., Grossman, J.N., and Garvie, L. (2014) The Meteoritical Bulletin, no. 100, 2014 June. Meteoritics & Planetary Science, 49 (8), E1-E101.

Sarafian, A.R., Roden, M.F., and Patiño-Douce, A.E. (2013) The volatile content of Vesta: Clues from apatite in eucrites. Meteoritics & Planetary Science, 48 (11), 2135-2154.

Sarafian, A.R., John, T., Roszjar, J. and Whitehouse, M.J. (2017) Chlorine and hydrogen degassing in Vesta's magma ocean. Earth and Planetary Science Letters 459, 311-319.

Van Schmus, W.R., and Ribbe, P.H. (1969) Composition of phosphate minerals in ordinary chondrites. Geochimica et Cosmochimica Acta, 33 (5), 637–640.

Scott, E.R., and Bild, R.W. (1974) Structure and formation of the San Cristobal meteorite, other IB irons and group IIICD. Geochimica et Cosmochimica Acta, 38 (9), 1379–1391.

Sepp, B., Bischoff, A., and Bosbach, D. (2001) Low-temperature phase decomposition in iron-nickel metal of the Portales Valley meteorite. Meteoritics & Planetary Science, 36 (5), 587–595.

Shearer, C.K., Burger, P.V., Papike, J.J., McCubbin, F.M., and Bell, A.S. (2015) Crystal chemistry of merrillite from Martian meteorites: Mineralogical recorders of magmatic processes and planetary differentiation. Meteoritics & Planetary Science, 50 (4), 649–673.

Sokol, A.K., Bischoff, A., Marhas, K.K., Mezger, K., and Zinner, E. (2007a) Late accretion and lithification of chondritic parent bodies: Mg isotope studies on fragments from primitive chondrites and chondritic breccias. Meteoritics & Planetary Science 42, 1291-1308.

Sokol, A.K., Mezger, K., Chaussidon, M. and Bischoff, A. (2007b) Simultaneous accretion of differentiated or metamorphosed asteroidal clasts and chondrules. Meteoritics & Planetary Science 42, A143.

Stelzener, T., Heide, K., Bischoff, A., Weber, D., Scherer, P., Schultz, L., Happel, M., Schrön, W., Neupert, U., Michel, R., Clayton, R.N., Mayeda, T.K., Bonani, G., Haidas, I., Ivy-Ochs, S., and Suter, M. (1999) An interdisciplinary study of weathering effects in ordinary chondrites from the Acfer region, Algeria. Meteoritics & Planetary Science, 34 (5), 787–794.

Stöffler, D., Keil, K., and Scott, E.R.D. (1991) Shock metamorphism of ordinary chondrites. Geochimica et Cosmochimica Acta, 55 (12), 3845–3867.

Stolper, E. (1977) Experimental petrology of eucritic meteorites. Geochimica et Cosmochimica Acta, 41 (5), 587–611.

1222 Terada K., and Bischoff A. (2009) Asteroidal granite-like magmatism 4.53 Gyr ago. The
1223 Astrophysical Journal 699, L68-L71.
1224 Terada, K., and Sano, Y. (2004) Ion microprobe U-Th-Pb dating and REE analyses of phosphates in
1225 the Nakhlites Lafayette and Yamato-000593/000749. Meteoritics & Planetary Science, 39 (12),
1226 2033–2041.
1227 Wadhwa, M., McSween, H.Y., and Crozaz, G. (1994) Petrogenesis of shergottite meteorites inferred
1228 from minor and trace element microdistributions. Geochimica et Cosmochimica Acta, 58 (19),
1229 4213–4229.
1230 Ward, D., Roszjar, J., Bischoff, A., and Leschner, L. (2014) Accessory Ca-phosphates in meteorites –
1231 distribution and composition (abstract MET-P01). DMG-Meeting Jena, 210.
1232 Ward, D., Bischoff, A., Roszjar, J., and Whitehouse, M.J. (2015) REE content of meteoritic Ca-
1233 phosphates. Meteoritics & Planetary Science 50, Special Issue, #5056.
1234 Ward, D., Bischoff, A., Roszjar, J., and Whitehouse, M.J. (2016) Trace element inventory of
1235 meteoritic Ca-phosphates. Lunar and Planetary Science, XLVII, abstract 1456.
1236 Warren, P.H., Greenwood, J.P., and Rubin, A.E. (2004) Los Angeles: A tale of two stones.
1237 Meteoritics & Planetary Science, 39 (1), 137–156.
1238 Wasson, J.T. (1974) Meteorites: Classification and Properties, 316p. Springer-Verlag, Berlin.
1239 Watson, E.B. (1979) Apatite saturation in basic to intermediate magmas. Geophysical Research
1240 Letters, 6 (12), 937–940.
1241 Weisberg, M.K., Smith, C., Benedix, G.K., Folco, L., Righter, K., Zipfel, J., Yamagushi, A., and
1242 Aoudjehane, H.C. (2008) The Meteoritical Bulletin, no. 94, September 2008. Meteoritics &
1243 Planetary Science, 43 (9), 1551–1584.
1244 Wittke, J.H., Bunch, T.E., Irving, A.J., Farmer, M., and Strope, J. (2006) Northwest Africa 2975: an
1245 evolved basaltic shergottite with vesicular glass pockets and trapped melt inclusions. Lunar and
1246 Planetary Science, XXXVII, abstract 1368.
1247 Whitehouse, M.J., Kamber, B.S., and Moorbath, S. (1999) Age significance of U–Th–Pb zircon data
1248 from early Archaean rocks of West Greenland - a reassessment based on combined ion-
1249 microprobe and imaging studies. Chemical Geology, 160 (3), 201–224.
1250 Wlotzka, F. (1993) The Meteoritical Bulletin, no. 74, Meteoritics, 28 (1), 146–153.
1251 Yagi, K., Lovering, J.F., Shima, M., and Okada, A. (1978) Petrology of the Yamato meteorites (j), (k),
1252 (l), and (m) from Antarctica. Meteoritics, 13 (1), 23–45.

Yamaguchi, A., Takeda, H., Bogard, D.D., and Garrison, D. (1994) Textural variations and impact history of the Millbillillie eucrite. Meteoritics 29 (2), 237–245.

Yang, S., Humayun, M., Jefferson, G., Fields, D., Righter, K., and Irving, A.J. (2013) Chemical composition of four shergottites from Northwest Africa (NWA 2800, NWA, 5214, NWA 5990, NWA 6342). Lunar and Planetary Science, XLIV, abstract 1738.

Xie, X., Yang, H., Gu, X., and Downs, R.T. (2015) Chemical composition and crystal structure of merrillite from the Suizhou meteorite. American Mineralogist, 100 (11-12), 2753–2756.

Zhang, A., and Yurimoto, H. (2013) Petrography and mineralogy of the ungrouped type 3 carbonaceous chondrite Dar al Gani 978. Meteoritics & Planetary Science, 48 (9), 1651–1677.

Zipfel, J., Palme, H., Kennedy, A.K., and Hutcheon, I.D. (1995) Chemical composition and origin of the Acapulco meteorite. Geochimica et Cosmochimica Acta, 59 (17), 3607–3627.

Zipfel, J., Scherer, P., Spettel, B., Dreibus, G., and Schultz, L. (2000) Petrology and chemistry of the new shergottite Dar al Gani 476. Meteoritics & Planetary Science, 35 (1), 95–106.

Supplementary Material

SUPPLEMENTARY TABLE S1.	Individual phosphate analyses, provided in an excel spreadsheet.
SUPPLEMENTARY TABLE S2.	Analyzed additional reference material, provided in an excel spreadsheet.
SUPPLEMENTARY TABLE S3.	Composition of the Durango apatite and comparison to literature data.
SUPPLEMENTARY TABLE S4.	Average REE concentrations of the major REE carrier phases in ALM-A.
SUPPLEMENTARY TABLE S5.	Mass balance calculations for Sm in achondrites.
SUPPLEMENTARY FIG. S1	Apatite with labeled SIMS and LA-ICP-MS spots and corresponding REE patterns
SUPPLEMENTARY FIG. S2	Bulk range of the Na_2O vs P_2O_5 content from the meteorite groups analyzed.
SUPPLEMENTARY FIG. S3	REE + Y vs. Na (apfu).

List of figure captions

Figure 1. Back-scattered electron (BSE) images of Ca-phosphates at the metal-sulfide interface. Phase abbreviations: Ap = apatite, Mer = merrillite, Px = low-Ca pyroxene, Plg = plagioclase, Ol = olivine, FeS = iron-sulfide, Kam = kamacite, Tae = taenite, Chr = chromite, Mag = magnetite. **(a)** Both phosphate species associated with the Fe-Ni-alloys kamacite and taenite. **(b)** Merrillite assembled with Fe-sulfide, chromite, olivine, and Fe-Ni alloys. **(c)** Large apatite-pyroxene and merrillite inclusions within the metal phase. The small white areas are remnants of prior gold coating and not indigenous to the sample. **(d)** Apatite inclusion within magnetite-sulfide.

Figure 2. BSE images of silicate assemblages with Ca-phosphates. Phase abbreviations: Ap = apatite, Mer = merrillite, Px = low-Ca pyroxene, Plg = plagioclase, Ol = olivine, Fsp = feldspar, SiO_2 = silica polymorph, FeS = iron-sulfide, Kam = kamacite, Tae = taenite, (Ti-)Mag = (Ti-)magnetite, Ilm = ilmenite, Sp = spinel. **(a)** Apatite located among plagioclase, low-Ca pyroxene and olivine. **(b)** Merrillite grains enveloping a CAI. **(c)** Fragment composed of pyroxene, plagioclase, and apatite with small magnetite inclusions. **(d)** Lath-shaped apatite in paragenesis with pyroxene and feldspar. **(e)** Merrillite grain with a thin apatite rim in one corner facing a silica polymorph, which also occurs as inclusions within the merrillite. It is associated with pyroxene and plagioclase. **(f)** Large merrillite grain with inclusions of plagioclase, olivine, ilmenite, Ti-magnetite and SiO_2-polymorph, located within a symplectite area (Llorca et al. 2013).

Figure 3. Mineral assemblages of Ca-phosphates in the Adzhi-Bogdo (stone) LL3-6 chondritic breccia. Phase abbreviations: Ap = apatite, Mer = merrillite, Px = low-Ca pyroxene, Plg = plagioclase, KFsp = K-feldspar, Ol = olivine, SiO_2 = silica polymorph, FeS = iron-sulfide, Kam = kamacite, Tae = taenite, Chr = chromite, Ilm = ilmenite. **(a)** Merrillite in contact with chromite, olivine, pyroxene and plagioclase in a chondritic, strongly recrystallized type 6 fragment. **(b)** Apatite

1299 with small olivine inclusions (mostly <5 μm) in a similar highly metamorphic association. **(c)**
1300 Subhedral to anhedral apatite at the corner of an "achondritic fragment" consisting of K-feldspar
1301 and plagioclase embedded in the fine-grained, clastic matrix. The small white spots are remnants of
1302 past gold-coating of the section. **(d)** Euhedral and subhedral apatite grains within an "achondritic
1303 fragment" dominated by silica polymorph and K-feldspar.

1304 **Figure 4.** Chemical variation of MgO and FeO (a and b) vs. Na_2O (c and d) for merrillite (a
1305 and c) and apatite (b and d). Each point illustrates a single analysis: circles and diamonds represent
1306 apatite, while triangles and squares correspond to merrillite.

1307 **Figure 5.** Ternary plots of anion abundances in apatite within the different meteorite
1308 groups. Points correspond to individual analyses from this study, while the shaded areas illustrate the
1309 ranges of data published by Patiño-Douce and Roden (2006), Sarafian et al. (2013), Zhang and
1310 Yurimoto (2013), Jones et al. (2014), McCubbin et al. (2014), Dyl et al. (2015) and McCubbin and
1311 Jones (2015). Restricted variation is observed for most meteorite types, with Cl-rich apatite in
1312 undifferentiated samples (a and b) and F-rich apatite in primitive achondrites and other differentiated
1313 meteorites (c), except for Martian samples, which show a lot of scatter (d).

1314 **Figure 6.** Apatite REE abundances in chondrites normalized to bulk CI chondrite
1315 (Barrat et al. 2012); individual analyses are available in the supplement (Tab. S1). Colored fields mark
1316 the ranges obtained by all analyses of the same phosphate species within the context of this study;
1317 lines within the fields represent the average. Gray areas indicate literature data from Bremervörde
1318 (H4), Forest Vale (H4), Beaver Creek (H4), Alta'ameem (LL5), Guidder (LL5), St.Severin (LL6) and
1319 Uden (LL6) from Crozaz et al. (1989). Apatite REE-patterns **(a)** with positive Eu anomalies in
1320 Devgaon (H3.8) and Portales Valley (H6); **(b)** without pronounced Eu anomaly in Ybbsitz (H4),
1321 Bruderheim (L6), and Villalbeto de la Peña (L6); **(c)** with enrichment in Ce and Pr from the

Karoonda CK4 carbonaceous chondrite; **(d)** in the Adzhi-Bogdo LL3-6 regolith breccia. The purple field marks the range in the chondritic portion consistent with patterns of other ordinary chondrites shown in (b). Colored lines correspond to single analyses of apatite located in the achondritic fragments, each color representing a different fragment. Apatite from these fragments is more enriched (~100-250 × CI) and has flat REE patterns with negative Eu anomalies, similar to patterns observed in achondrites (Fig.7).

Figure 7. Apatite REE abundances in achondrites normalized to CI chondrite (Barrat et al. 2012); individual analyses are available in the supplement (Tab. S1). Colored fields mark the range obtained by all analyses of the same phosphate species within this study; lines within the fields represent the average. Gray areas mark available literature data for the corresponding samples or meteorite groups. Apatite REE-patterns from **(a)** the acapulcoites Dhofar 125 and Acapulco, relative to literature data from Zipfel et al. (1995); **(b)** the winonaite HaH 193 and the ureilitic trachyandesite ALM-A. Apatite REE-patterns from both samples resemble those of (a). While ALM-A apatite exhibits a more pronounced slope from La to Lu, HaH 193 apatite shows a much higher spread of overall REE-enrichment (but consistent pattern shapes); **(c)** the eucrites NWA 5073 and Millbillillie, and Landes IAB iron meteorite. The gray area marks the range of eucritic apatite documented by Hsu and Crozaz (1996).

Figure 8. Merrillite REE abundances normalized to CI chondrite (Barrat et al. 2012); individual analyses are available in the supplement (Tab. S1). The colored fields mark the range obtained by all analyses of the same phosphate species, lines correspond to the average of the given field, except in (a). Gray areas illustrate available literature data for the corresponding meteorite groups or samples. **(a)** The average of each sample is illustrated by the numbered solid lines (#1-6). The patterns are generally aligned with literature data from Crozaz et al. (1989), yet Ybbsitz (#5) and Portales Valley (#6) are less REE-enriched. **(b)** Merrillite REE data for acapulcoites and the

Millbillillie eucrite, relative to literature data from Zipfel et al. (1995) for acapulcoites (light gray) and Hsu and Crozaz (1996) for eucrites (dark gray); both are in good agreement with the obtained data. **(c)** REE patterns in Dalgaranga (purple field) and Bondoc (green field) mesosiderites, as well as from the Landes IAB silicate iron meteorite (red field). Data for mesosiderites Vaca Muerta, Emery, and Morristown (Crozaz et al. 1985) are outlined in gray, with the individual patterns from these samples displayed as the gray, dotted lines.

Figure 9. Merrillite REE abundances in shergottites normalized to CI (Barrat et al. 2012); individual analyses are available in the supplement (Tab. S1). The colored fields mark the range of all merrillite analyses; the solid lines correspond to the average of the given sample. The gray areas are literature data for the corresponding subtype after Shearer et al. (2015); **(a)** from the depleted shergottites DaG 1051 (purple) and SaU 005 (yellow). Dotted lines correspond to whole rock REE patterns by Folco et al. (2000; note that the pattern illustrates data on DaG 476 which is paired with DaG 1051) and Dreibus et al. (2000; SaU 005); **(b)** from the enriched shergottites Zagami (blue) and NWA 4864 (magenta). Both dotted lines correspond to whole rock REE patterns by Barrat et al. (2001; Zagami) and Bendel (2013; NWA 4864).

Figure 10. CI-normalized non-REE trace element abundances in **(a)** apatite and **(b)** merrillite from chondrites. Data are presented relative to CI from Barrat et al. (2012) and sorted by atomic number. The abundances do not correlate with the petrologic type of the host chondrite in either species, yet apatite shows more variation, especially considering Sc – Y, when compared with merrillite.

1367 **Figure 11.** CI-normalized (Barrat et al. 2012) non-REE trace element abundances in **(a)**
1368 primitive achondrites and (**b-d**) differentiated meteorites (mesosiderites, eucrites and shergottites). In
1369 contrast to the REE, the remaining trace elements are not universally enriched in merrillite when
1370 compared to apatite, if both are present in the same sample.

1371 **Figure 12.** Positive correlation of apatite U vs. Th concentrations, given in µg/g
1372 among different meteorites and planetary bodies. Note that both abundances increase with the grade
1373 of metamorphism (petrologic type) and with the degree of differentiation of the respective parent
1374 body. Colored areas represent literature data for Lunar (blue), Martian (orange) and mafic terrestrial
1375 (gray) apatite by Nemchin et al. (2009), Terada and Sano (2004), and O'Reilly and Griffin (2000)
1376 respectively.

1377 **Figure 13.** Average REE concentrations of the main REE carrier phases in the
1378 ALM-A ureilitic trachyandesite. The bulk rock REE pattern is calculated based on REE averages of
1379 each phase (details in supplemental table S4) and the modal abundances given by Bischoff et al.
1380 (2014).
1381
1382
1383

This is a preprint, the final version is subject to change, of the American Mineralogist (MSA)
Cite as Authors (Year) Title. American Mineralogist, in press.
(DOI will not work until issue is live.) DOI: http://dx.doi.org/10.2138/am-2017-6056

Tables

TABLE 1: Details of the analyzed Ca-phosphate bearing meteorites from the sample suite.

group	subgroup	type	sample	sample id	discovery	shock	weathering	literature	bulk P_2O_5 wt%	modal abundance vol%[+]	Ap	Mer	ratio[**] Ap/Mer
Ordinary chondrites	**H**	3.8	**Devgaon**	PL15259	fall	S2	W0	a		0.18*	yes	yes	1:1.75
	H	4	**Ybbsitz**	PL89476	find	S2	W1	b			yes	yes	2:1
	H	5	**Allegan**	PL00252	fall	S1	W0	c	0.27[y]		no	yes	
	H	6	**Portales Valley**	PL99051	fall	S2	W0	d		2.95[z]	yes	yes	1:1.5
	L	3.8	**Aguemour 009**	PL92311	find	S3	W1	e				yes	
	L	6	**Bruderheim**	PL90272	fall	S4	W0	f	0.21[y]		yes	yes	2:1
	L	6	**Villalbeto de la Peña**	PL13067 PL13068	fall	S4	W0	g		0.31*	yes	Yes	1:2
	LL	3-6	**Adzhi-Bogdo (stone)**	PL92505 A PL92505 C PL02135	fall	S2	W2	h		0.29*	yes	yes	2.5:1
Carbonaceous chondrite	**CK**	4	**Karoonda**	PL89180	fall	S1	W0	i			yes	no	
Acapulcoites			**Acapulco**	PL11017 PL11018	fall	S2	W0	j	1.0[j] - 1.6[aa]	< 1.1*	yes	yes	2:1
			Dhofar 125	PL01019	find	S1	W1-2	k		0.65*	yes	no	
			NWA 1052	PL02138	find	S1	W2-3	l		0.85*	no	yes	
Winonaite			**HaH 193**	PL96276	find	S1	W3	m		0.1 - 0.3[m]	yes	no	
HED	eucrites		**NWA 5073**	PL15260	find	S2	W2-3	n		< 0.1*	yes	yes	4:1
			Millbillillie	PL89504	fall	S3	W0/1	o		< 0.1*	yes	yes	3:1
Martian meteorites	shergottites	depleted	**SaU 005**	PL00123	find	S5	W1	p	0.31[p]	0.24*	no	yes	
			DaG 1051	PL09224	find	S5	W1	q	0.32[ab] - 0.49[q]	0.69* - 1[ac]	no	yes	
		enriched	**Zagami**	PL97001	fall	S5	W0	r	0.5[ad] - 0.58[ae]	0.6 - 1.2[ae]	yes	yes	1:2
			KG 002	PL11155	find	S5	W2-3	s	1.5[s]	2.7[s]	yes	yes	1:2
			NWA 4864	PL08011	find	S5	W1	t	1.45[af]	1.7[ag]	yes	yes	1:3
Ureilite	trachyandesite (ALM-A)		**Almahata Sitta**	PL13030	fall	S2	W0	u	0.52[u]	0.95*	yes	yes	
Stony irons	Mesosiderites	(A3)	**Dalgaranga**	PL05175	find	S2	W3	v		1* - 3.4[ah]	no	yes	
		(B4)	**Bondoc**	PL05176	find	S2	W3	w		0.2[ah]	no	yes	
Iron meteorite	IAB		**Landes**	PL15257 PL15258	find	*no PTS*	*no PTS*	x	0.24[x]		yes	yes	

Ap = apatite; Mer = merrillite; NWA = Northwest Africa; HaH = Hammadah al Hamra; SaU = Sayh al Uhaymir; DaG = Dar al Gani; KG = Ksar Ghilane; PTS = polished thin section; [+] = modal abundance of both Ca-phosphate species combined; * = obtained from SEM mappings, see text for details.** = Ca-phosphate grains were identified at the SEM. The ratio corresponds to the number of the identified grains, if modal abundances of individual species are available, they are listed in supplemental Table S5.
Shock stages were determined based on Stöffler et al. (1991) for ordinary chondrites.

References: a) Murty et al. 2004; b) Kiesl 1981; c) Easton and Elliot 1977; d) Sepp et al. 2001; e) Wlotzka, 1993; f) Haas & Haskin 1991; g) Dyl et al. 2012; Bischoff et al. 2013; h) Bischoff et al. 1993; i) Fitzgerald 1979; j) Palme et al. 1981; Zipfel et al 1995; Min et al. 2003 k) Greshake et al. 2001; l) Moggi-Cecchi et al. 2005; m) Floss et al. 2007; n) Roszjar et al. 2011; o) Yamaguchi et al. 1994; p) Dreibus et al. 2000; q) Folco et al. 2000 *on DaG 489, paired with DaG 1051*; r) McCoy et al. 1992; s) Llorca et al. 2013; t) Weisberg et al. 2008; Ruzicka et al. 2014; u) Bischoff et al. 2014; Horstmann & Bischoff 2014; v) Delaney et al. 1980; Nehru et al. 1980; w) Powell 1971; x) Bunch et al. 1972; Herpfer et al. (1994); y) Jarosewich 1990; z) Ruzicka et al. 2005; aa) Mittlefehldt 2007; ab) Zipfel et al. 2000; ac) Mikouchi et al. 2001 *on DaG 476 paired with DaG 1051*; ad) Lodders 1998; ae) McCoy et al. 1992; af) Yang et al. 2013 *on NWA 5214, paired with NWA 4864*; ag) Wittke et al. 2006 *on NWA 2975, paired with NWA 4864)*; ah) Prinz et al. 1980;

This is a preprint, the final version is subject to change, of the American Mineralogist (MSA)
Cite as Authors (Year) Title. American Mineralogist, in press.
(DOI will not work until issue is live.) DOI: http://dx.doi.org/10.2138/am-2017-6056

1386 **Table 2a.** Average apatite composition ±SD in wt%, obtained by EPMA. Individual analyses are available within the supplementary material.

Ap	Devgaon (n= 7)	Ybbsitz (n= 4)	Portales Valley (n=3)	Bruderheim (n=7)	Villalbeto de la Peña (n=4)	Adzhi-Bogdo (chondr.portion) (n= 5)	Adzhi-Bogdo (diff.clasts) (n= 3)	Karoonda (n= 3)	Acapulco (n=9)	Dhofar 125 (n= 4)	HaH 193 (n= 8)	NWA 5073 (n=3)	Millbillillie (n=3)	NWA 4864 (n= 3)	ALM-A (n= 6)	Landes (n= 1)
CaO	53.30 ± 0.58	52.07 ± 0.78	53.13 ± 0.07	53.32 ± 0.25	53.41 ± 0.13	53.48 ± 0.53	51.60 ± 0.34	53.24 ± 0.67	54.58 ± 0.27	54.18 ± 0.42	54.67 ± 0.83	53.41 ± 0.48	54.36 ± 1.32	53.54 ± 0.22	52.36 ± 0.22	53.69
Na_2O	0.36 ± 0.09	0.31 ± 0.03	0.48 ± 0.01	0.36 ± 0.03	0.40 ± 0.04	0.22 ± 0.05	0.26 ± 0.07	0.06 ± 0.03	0.14 ± 0.04	0.16 ± 0.05	<0.06	<0.06	<0.06	0.11 ± 0.03	0.58 ± 0.04	0.46
SrO	0.13 ± 0.03				0.08 ± 0.01			<0.08	0.11 ± 0.02	0.13 ± 0.03	0.10 ± 0.02	0.08 ± 0.02	<0.08 ± 0.04		0.13 ± 0.02	
Cr_2O_3	<0.06	0.06 ± 0.01	<0.06	<0.06	<0.06	<0.06	0.08 ± 0.03	0.11 ± 0.05	<0.06	<0.06	<0.06	<0.06	<0.06		<0.06	<0.06
FeO	0.42 ± 0.21	1.06 ± 0.32	0.41 ± 0.08	0.12 ± 0.04	0.33 ± 0.28	0.40 ± 0.3	0.14 ± 0.4	1.23 ± 0.49	0.13 ± 0.06	0.59 ± 0.26	1.03 ± 0.46	0.78 ± 0.12	0.55 ± 0.10	0.87 ± 0.11	0.78 ± 0.06	<0.07
MnO	<0.06	0.07 ± 0.02	0.09 ± 0.03	<0.06	<0.06	<0.06		0.06 ± 0.04	0.10 ± 0.02	0.06 ± 0.01	<0.05	0.05 ± 0.01	<0.05	0.18 ± 0.05	0.20 ± 0.01	0.11
MgO	0.08 ± 0.04	0.08 ± 0.01	<0.05	<0.05	<0.05	0.07 ± 0.4	<0.05	0.21 ± 0.07	0.21 ± 0.03	0.29 ± 0.01	0.21 ± 0.04	<0.09 ± 0.07	0.05 ± 0.01	<0.05	0.43 ± 0.02	0.16
P_2O_5	40.81 ± 0.56	39.99 ± 0.27	41.62 ± 0.05	41.11 ± 0.36	40.84 ± 0.44	42.05 ± 1.03	40.75 ± 0.17	39.61 ± 1.22	42.58 ± 0.39	41.69 ± 0.06	41.81 ± 0.57	40.28 ± 0.34	41.48 ± 0.45	40.92 ± 0.38	41.21 ± 0.17	42.07
SiO_2	<0.05	0.39 ± 0.20		0.05 ± 0.03	0.07 ± 0.01	0.21 ± 0.10	0.51 ± 0.15	0.56 ± 0.25	0.06 ± 0.02	0.09 ± 0.01	<0.03 ± 0.01	1.05 ± 0.60	0.17 ± 0.11	0.45 ± 0.09	0.26 ± 0.04	<0.05
SO_3	<0.07	<0.07	<0.07	<0.07	<0.07	<0.07	0.07 ± 0.02	<0.07	<0.07	<0.07	<0.07	<0.07	<0.07		<0.07	
TiO_2	<0.08	b.d.	<0.08	<0.08	<0.08	<0.08	0.08 ± 0.02	<0.08	<0.08	<0.08	<0.08	<0.08	0.26 ± 0.09		<0.08	
Al_2O_3	<0.03	0.07 ± 0.03	<0.03	<0.03	<0.03	0.03 ± 0.02	0.10 ± 0.01	<0.03	<0.03	<0.03	<0.03	<0.03	0.38 ± 0.28	0.04 ± 0.01	<0.03	<0.03
Cl	5.48 ± 0.15	4.93 ± 0.14	5.62 ± 0.03	5.46 ± 0.13	5.12 ± 0.27	6.08 ± 0.27	6.62 ± 0.05	4.44 ± 0.74	1.75 ± 0.10	1.29 ± 0.33	0.72 ± 0.06	0.29 ± 0.03	0.20 ± 0.02	4.15 ± 0.71	3.10 ± 0.04	5.61
F	0.50 ± 0.07	0.54 ± 0.14	0.28 ± 0.06	0.43 ± 0.11	0.69 ± 0.03	0.18 ± 0.04	0.17 ± 0.04	0.56 ± 0.05	3.01 ± 0.17	3.35 ± 0.36	4.06 ± 0.34	3.54 ± 0.15	3.70 ± 0.35	0.93 ± 0.40	1.54 ± 0.12	0.62
H_2O*	0.10 ± 0.07	0.20 ± 0.05	0.19 ± 0.02	0.14 ± 0.07	0.10 ± 0.07	0.13 ± 0.06	0.00	0.31 ± 0.19	0.01 ± 0.01	0.00	0.00	0.03 ± 0.02	0.06 ± 0.05	0.25 ± 0.09	0.23 ± 0.05	0.05
total	**101.12**	**99.56**	**101.62**	**100.85**	**100.93**	**102.75**	**100.44**	**100.09**	**102.67**	**101.86**	**102.69**	**99.68**	**101.22**	**101.19**	**100.59**	**102.72**
corrected O = F + Cl	*99.74*	*98.22*	*100.24*	*99.44*	*99.49*	*101.30*	*98.87*	*98.85*	*101.00*	*100.16*	*100.82*	*98.13*	*99.62*	*99.86*	*99.25*	*101.19*
Ca	9.90 ± 0.13	9.82 ± 0.17	9.79 ± 0.01	9.89 ± 0.06	9.96 ± 0.06	9.74 ± 0.10	9.63 ± 0.09	9.70 ± 0.36	9.76 ± 0.05	9.79 ± 0.04	9.79 ± 0.11	9.82 ± 0.16	9.82 ± 0.12	9.88 ± 0.02	9.65 ± 0.03	9.76
Na	0.12 ± 0.03	0.11 ± 0.01	0.16 ± 0.01	0.12 ± 0.01	0.13 ± 0.01	0.07 ± 0.02	0.09 ± 0.03	0.02 ± 0.01	0.04 ± 0.01	0.05 ± 0.02	b.d.	b.d.	b.d.	0.04 ± 0.01	0.19 ± 0.01	0.15
Sr	<0.01				<0.01			<0.01	<0.01	<0.01	<0.01	<0.01	<0.01		<0.01	
Cr	b.d.	<0.01	b.d.	b.d.	b.d.	<0.02	< 0.01	0.02	b.d.	b.d.	b.d.	b.d.	b.d.		b.d.	b.d.
Fe	0.06 ± 0.03	0.15 ± 0.05	0.06 ± 0.01	0.02 ± 0.01	0.05 ± 0.03	0.06 ± 0.04	0.02 ± 0.01	0.43 ± 0.41	0.02 ± 0.01	0.08 ± 0.04	0.14 ± 0.06	0.11 ± 0.02	0.08 ± 0.01	0.13 ± 0.02	0.11 ± 0.01	b.d.
Mn	b.d.	<0.01	<0.01	b.d.	b.d.	b.d.		0.01 ± 0.01	<0.02	<0.01	<0.01	<0.01	<0.01	0.03 ± 0.01	0.03 ± 0.01	0.02
Mg	<0.02	<0.02	b.d.	b.d.	b.d.	0.02 ± 0.01	b.d.	0.05 ± 0.02	0.05 ± 0.01	0.07 ± 0.01	0.05 ± 0.01	0.02 ± 0.02	b.d.	b.d.	0.11 ± 0.01	0.04
P	5.99 ± 0.05	5.96 ± 0.04	6.06 ± 0.01	6.03 ± 0.04	6.02 ± 0.02	6.05 ± 0.06	6.01 ± 0.02	5.89 ± 0.12	6.02 ± 0.03	5.96 ± 0.02	5.92 ± 0.04	5.85 ± 0.02	5.92 ± 0.03	5.97 ± 0.02	6.00 ± 0.02	6.05
Si	<0.02	0.07 ± 0.03		<0.01	<0.01	0.04 ± 0.02	0.09 ± 0.03	0.10 ± 0.05	<0.01	0.02 ± 0.01	<0.01	0.18 ± 0.10	0.03 ± 0.02	0.08 ± 0.01	0.05 ± 0.01	b.d.
S	b.d.	b.d.	b.d.	b.d.	b.d.	b.d.	<0.01	b.d.	b.d.	b.d.	b.d.	<0.01	<0.01		b.d.	
Ti	b.d.	b.d.	b.d.	b.d.	b.d.	b.d.	<0.01	b.d.	b.d.	b.d.	b.d.	<0.01	0.03 ± 0.01		b.d.	
Al	b.d.	<0.02	b.d.	b.d.	b.d.	<0.01	0.02 ± 0.01	b.d.	b.d.	b.d.	b.d.	b.d.	0.08 ± 0.06	<0.01	b.d.	b.d.
Cl	1.61 ± 0.05	1.47 ± 0.06	1.64 ± 0.01	1.60 ± 0.04	1.50 ± 0.09	1.75 ± 0.07	1.95 ± 0.02	1.32 ± 0.23	0.50 ± 0.03	0.37 ± 0.10	0.20 ± 0.01	0.08 ± 0.01	0.06 ± 0.01	1.21 ± 0.21	0.90 ± 0.01	1.61
F	0.27 ± 0.04	0.30 ± 0.08	0.15 ± 0.03	0.24 ± 0.06	0.41 ± 0.06	0.10 ± 0.02	0.10 ± 0.02	0.31 ± 0.03	1.59 ± 0.08	1.79 ± 0.19	2.15 ± 0.19	1.92 ± 0.07	1.88 ± 0.05	0.50 ± 0.22	0.84 ± 0.06	0.33
OH/other*	0.12 ± 0.08	0.23 ± 0.06	0.21 ± 0.03	0.16 ± 0.08	0.09 ± 0.09	0.15 ± 0.07	0.00	0.36 ± 0.21	0.02 ± 0.01			0.03 ± 0.04	0.06 ± 0.05	0.28 ± 0.10	0.26 ± 0.06	0.06
cations	**16.11**	**16.15**	**16.07**	**16.06**	**16.18**	**15.98**	**15.88**	**16.21**	**15.93**	**16.00**	**15.90**	**16.01**	**15.97**	**16.12**	**16.15**	**16.02**
X-Site																
X_{Cl}	0.81 ± 0.02	0.73 ± 0.03	0.81 ± 0.01	0.80 ± 0.02	0.75 ± 0.04	0.88 ± 0.04	0.95 ± 0.01	0.66 ± 0.12	0.24 ± 0.02	0.17 ± 0.05	0.09 ± 0.01	0.04 ± 0.01	0.03 ± 0.01	0.61 ± 0.11	0.45 ± 0.01	0.81
X_F	0.14 ± 0.02	0.15 ± 0.04	0.08 ± 0.02	0.12 ± 0.03	0.21 ± 0.03	0.05 ± 0.01	0.05 ± 0.01	0.16 ± 0.01	0.75 ± 0.02	0.83 ± 0.05	0.91 ± 0.01	0.94 ± 0.02	0.94 ± 0.02	0.25 ± 0.11	0.42 ± 0.03	0.16
$X_{OH/other}$	0.06 ± 0.04	0.12 ± 0.03	0.11 ± 0.01	0.08 ± 0.04	0.05 ± 0.05	0.07 ± 0.03	0.00 ± 0.00	0.18 ± 0.11	0.01 ± 0.01	0.00 ± 0.00	0.00 ± 0.00	0.02 ± 0.01	0.03 ± 0.02	0.14 ± 0.05	0.13 ± 0.03	0.03

Notes: b.d. = below detection limit. |* = The H_2O/OH component was calculated based on ideal stoichiometric proportions (assuming an occupation of the apatite X-site with 2.00 atoms per formula unit with F+Cl+OH). Hence, this fraction may include substitutions or vacancies in the apatite crystal structure. See Text for details.

Detection limits 3σ above bg in wt%: CaO: 0.05; Na_2O: 0.06; SrO: 0.08; Cr_2O_3: 0.06; FeO: 0.07; MnO: 0.06; MgO: 0.05; P_2O_5: 0.07; SiO_2: 0.05; SO_3: 0.07; TiO_2: 0.08; Al_2O_3: 0.03; Cl: 0.06; F: 0.12

Errors in %: Ca: 0.6; Na: 8.4; Sr: 14.9; Cr: 19.5; Fe: 3.6; Mn: 12.5; Mg: 6.3; P: 1.6; Si: 6.6; S: 10.5; Ti: 7.7; Al: 4.5; Cl: 5.1; F: 5.6

1387

1388 **Table 2b.** Average merrillite composition in wt%, obtained by EPMA. Individual analyses are available within the supplementary material.

Mer	Devgaon (n=7)	Ybbsitz (n=3)	Allegan (n = 5)	Portales Valley (n=7)	Aguemour 009 (n=3)	Villalbeto de la Peña (n= 10)	Adzhi-Bogdo (n= 5)	Acapulco (n=7)	NWA 1052 (n= 3)	Millbillillie* (n= 2)	SaU 005 (n= 3)	DaG1051 (n=5)	NWA 4864 (n= 4)	Zagami (n= 11)	KG 002 (n= 4)	Dalgaranga (n= 5)	Bondoc (n= 12)	Landes (n= 1)
CaO	46.79 ± 0.52	46.87 ± 0.40	46.85 ± 0.22	46.76 ± 0.18	45.50 ± 0.05	46.63 ± 0.39	46.11 ± 0.42	46.53 ± 0.59	46.73 ± 0.20	42.89 ± 1.71	46.63 ± 0.60	47.78 ± 0.16	47.17 ± 0.20	46.49 ± 0.68	46.44 ± 0.31	43.99 ± 2.03	48.26 ± 0.20	47.09
Na_2O	2.86 ± 0.09	2.78 ± 0.06	2.77 ± 0.06	2.77 ± 0.04	2.71 ± 0.01	2.79 ± 0.09	2.63 ± 0.06	2.70 ± 0.12	2.63 ± 0.04	0.56 ± 0.18	1.74 ± 0.15	1.32 ± 0.17	1.35 ± 0.07	1.39 ± 0.08	1.15 ± 0.08	0.68 ± 0.08	0.95 ± 0.05	2.90
K_2O	0.04 ± 0.01	0.07 ± 0.01	0.05 ± 0.01	0.06 ± 0.01	0.07 ± 0.01	0.06 ± 0.01	0.04 ± 0.01	0.07 ± 0.03	0.07 ± 0.01	0.05 ± 0.01	<0.03			0.06 ± 0.02	0.12 ± 0.07	0.03 ± 0.01	0.07 ± 0.02	
SrO	0.09 ± 0.03					0.09 ± 0.03		0.09 ± 0.01	0.12 ± 0.02	0.08 ± 0.03	0.08 ± 0.01			0.10 ± 0.02		0.10 ± 0.03		
Cr_2O_3	<0.06	<0.06	<0.06	<0.06	0.13 ± 0.01	<0.06	0.07 ± 0.02	0.08 ± 0.04	<0.06	<0.06	<0.06	<0.06	<0.06	<0.06	0.07 ± 0.05	<0.06	<0.06	<0.06
FeO	0.61 ± 0.25	0.82 ± 0.26	0.32 ± 0.03	0.45 ± 0.07	0.48 ± 0.01	0.67 ± 0.18	0.66 ± 0.20	0.36 ± 0.08	0.39 ± 0.13	1.77 ± 0.12	1.04 ± 0.14	1.28 ± 0.07	3.31 ± 0.07	3.01 ± 0.26	4.78 ± 0.33	3.63 ± 1.31	0.78 ± 0.10	0.13
MnO	<0.06	<0.06	<0.06	<0.06	<0.06	<0.06		<0.06	<0.06	0.08 ± 0.02	<0.06	0.08 ± 0.03	0.17 ± 0.02	0.11 ± 0.02	<0.06	0.22 ± 0.02	0.07 ± 0.02	<0.06
MgO	3.61 ± 0.05	3.50 ± 0.03	3.57 ± 0.04	3.55 ± 0.03	3.37 ± 0.05	3.50 ± 0.09	3.54 ± 0.12	3.57 ± 0.15	3.59 ± 0.06	2.92 ± 0.10	3.56 ± 0.32	3.27 ± 0.03	2.04 ± 0.09	2.16 ± 0.12	0.88 ± 0.17	3.27 ± 0.10	3.52 ± 0.06	3.65
P_2O_5	45.96 ± 0.44	45.55 ± 0.46	46.72 ± 0.15	46.64 ± 0.34	47.14 ± 0.11	46.22 ± 0.42	46.64 ± 0.22	46.83 ± 0.24	46.47 ± 0.01	43.34 ± 0.53	45.34 ± 0.85	46.42 ± 0.40	45.85 ± 0.28	45.51 ± 0.98	45.73 ± 0.09	43.10 ± 2.07	46.37 ± 0.36	46.51
SiO_2	0.06 ± 0.03	0.35 ± 0.14	0.05 ± 0.03		0.20 ± 0.04	<0.05	0.28 ± 0.08	0.13 ± 0.10	<0.05	0.39 ± 0.07	0.07 ± 0.01	0.06 ± 0.02	0.12 ± 0.03	0.15 ± 0.08	0.54 ± 0.33	1.26 ± 0.96	0.19 ± 0.16	<0.05
SO_3	<0.07	<0.07	<0.07	<0.07	0.13 ± 0.03	<0.07	0.07 ± 0.04			0.08 ± 0.05	<0.07			<0.07	0.09 ± 0.04	0.60 ± 0.35	<0.07	
TiO_2	<0.08	<0.08	<0.08	<0.08	<0.08	<0.08	<0.08	<0.08	<0.08	0.12 ± 0.07	<0.08			<0.08	<0.08	<0.08	<0.08	
Al_2O_3	<0.03	0.04 ± 0.02	<0.03	<0.03	0.04 ± 0.01	<0.03	0.05 ± 0.02	<0.03	<0.03	<0.03	0.10 ± 0.08	<0.03	<0.03	<0.03	0.23 ± 0.10	0.45 ± 0.32	<0.03	<0.03
Cl	<0.06					<0.06		<0.06	<0.06	<0.06	<0.06	< 0.06	<0.01	<0.06	<0.06	<0.06		<0.06
total	**100.02**	**99.97**	**100.34**	**100.21**	**99.78**	**99.95**	**100.08**	**100.36**	**100.01**	**92.28**	**99.05**	**100.20**	**100.03**	**98.98**	**100.01**	**97.32**	**100.19**	**100.29**
Ca	17.96 ± 0.12	18.01 ± 0.04	17.83 ± 0.11	17.84 ± 0.12	17.32 ± 0.01	17.90 ± 0.15	17.53 ± 0.17	17.74 ± 0.28	17.86 ± 0.06	17.28 ± 0.35	18.05 ± 0.19	18.27 ± 0.09	18.24 ± 0.09	18.11 ± 0.12	17.99 ± 0.17	17.37 ± 0.49	18.47 ± 0.11	17.96
Na	1.98 ± 0.06	1.93 ± 0.03	1.91 ± 0.04	1.91 ± 0.03	1.87 ± <0.01	1.94 ± 0.06	1.80 ± 0.04	1.87 ± 0.10	1.82 ± 0.03	0.41 ± 0.14	1.22 ± 0.10	0.91 ± 0.11	0.94 ± 0.05	0.98 ± 0.06	0.80 ± 0.06	0.48 ± 0.05	0.66 ± 0.04	2.00
K	<0.02	0.03 ± <0.01	0.02 ± 0.01	0.03 ± 0.01	0.03 ± <0.01	0.03 ± 0.01	0.02 ± 0.01	0.03 ± 0.02	0.03 ± <0.01	0.02 ± <0.01	b.d.			0.03 ± 0.01	0.05 ± 0.03	<0.01	0.03 ±0.01	
Sr	0.02 ± 0.01					0.02 ± <0.01		0.02 ± <0.01	0.02 ± <0.01	0.02 ± <0.01	<0.01			0.02 ± 0.01		0.02 ± 0.01		
Cr	b.d.	b.d.	b.d.	b.d.	0.04 ± <0.01	b.d.	0.02 ± 0.01	0.02 ± <0.01	b.d.	b.d.	b.d.	b.d.	b.d.	b.d.	0.02 ± 0.01	b.d.	b.d.	b.d.
Fe	0.18 ± 0.07	0.25 ± 0.08	0.09 ± 0.01	0.13 ± 0.02	0.14 ± <0.01	0.20 ± 0.05	0.20 ± 0.06	0.11 ± 0.02	0.12 ± 0.04	0.56 ± 0.03	0.31 ± 0.04	0.38 ± 0.02	1.00 ± 0.02	0.92 ± 0.07	1.44 ± 0.10	1.13 ± 0.42	0.23 ± 0.03	0.04
Mn	b.d.	b.d.	b.d.	b.d.	b.d.	b.d.		b.d.	b.d.	0.03 ± <0.01	<0.02	0.02 ± 0.01	0.05 ± 0.01	0.04 ± 0.01	b.d.	0.07 ± 0.01	0.02 ± 0.01	b.d.
Mg	1.93 ± 0.03	1.87 ± 0.01	1.89 ± 0.02	1.88 ± 0.02	1.78 ± 0.03	1.87 ± 0.05	1.88 ± 0.06	1.89 ± 0.09	1.91 ± 0.03	1.64 ± 0.03	1.92 ± 0.18	1.74 ± 0.02	1.10 ± 0.05	1.17 ± 0.07	0.47 ± 0.09	1.80 ± 0.05	1.87 ± 0.03	1.93
P	13.93 ± 0.05	13.83 ± 0.05	14.05 ± 0.02	14.06 ± 0.06	14.18 ± 0.03	14.00 ± 0.06	14.04 ± 0.03	14.11 ± 0.04	14.04 ± 0.02	13.81 ± 0.10	13.87 ± 0.19	14.02 ± 0.04	14.01 ± 0.04	14.01 ± 0.11	13.99 ± 0.07	13.45 ± 0.40	14.02 ± 0.05	14.01
Si	0.02 ± 0.01	0.13 ± 0.05	<0.02		0.07 ± 0.01	b.d.	0.11 ± 0.03	0.05 ± 0.04	b.d.	0.15 ± 0.02	0.02 ± 0.01	0.02 ± 0.01	0.04 ± 0.01	0.05 ± 0.03	0.19 ± 0.12	0.47 ± 0.36	0.07 ±0.04	b.d.
S	b.d.	b.d.	b.d.	b.d.	0.03 ± 0.01	b.d.	0.04 ± 0.03			<0.05	b.d.			b.d.	0.05 ± 0.02	0.17 ± 0.10	b.d.	
Ti	b.d.	b.d.	b.d.	b.d.	b.d.	b.d.	b.d.	b.d.	b.d.	0.02 ± <0.01	b.d.			b.d.	b.d.	b.d.	b.d.	
Al	b.d.	0.02 ± 0.01	b.d.	b.d.	0.02 ± 0.01	b.d.	0.02 ± 0.01	<0.01	b.d.	b.d.	0.04 ±0.03	b.d.	<0.01	<0.01	0.07 ± 0.03	0.20 ± 0.14	b.d.	b.d.
Cl	b.d.					b.d.		b.d.	b.d.	b.d.	b.d.	b.d.	<0.01	b.d.	b.d.	b.d.		b.d.
total	**36.05**	**36.06**	**35.82**	**35.85**	**35.49**	**35.95**	**35.66**	**35.85**	**35.81**	**33.93**	**35.43**	**35.37**	**35.37**	**35.32**	**35.09**	**35.16**	**35.37**	**35.95**

Notes: b.d. = below detection limit. |* note, that eucritic merrillite contains several wt% of Y and REE (see text for details), therefore the totals of Millbillillie are low.
Detection limits 3σ above bg in wt%: CaO: 0.05; Na_2O: 0.06; K_2O: 0.03; SrO: 0.08; Cr_2O_3: 0.06; FeO: 0.07; MnO: 0.06; MgO: 0.05; P_2O_5: 0.07; SiO_2: 0.05; SO_3: 0.07; TiO_2: 0.08; Al_2O_3: 0.03; Cl: 0.06; F: 0.12
Errors in %: Ca: 0.6; Na: 8.4; K: 14.6; Sr: 14.9; Cr: 19.5; Fe: 3.6; Mn: 12.5; Mg: 6.3; P: 1.6; Si: 6.6; S: 10.5; Ti: 7.7; Al: 4.5; Cl: 5.1; F: 5.6

1389
1390
1391

1392 **Table 3.** REE concentration of apatite and merrillite. Results in µg/g (average and standard deviation of the mean
1393 (SD), individual analyses are available in supplemental table S1).

Sample		La	Ce	Pr	Nd	Sm	Eu	Gd	Tb	Dy	Ho	Er	Tm	Yb	Lu
Devgaon	apatite	12	25	3	11	2	2	3	0.5	3	0.6	2	0.2	1.6	0.20
	(n=7) SD	1	1	0.3	1	0.4	0.2	0.1	0.07	0.5	0.06	0.2	0.04	0.4	0.03
	merrrillite	28	83	11	49	12	2	17	3	18	4	12	1.7	11	1.6
	(n=7) SD	11	39	4	12	4	0.5	5	1	5	1	3	0.4	3	0.6
Ybbsitz	apatite	10	21	3	9	3	0.8	3	0.4	3	0.8	2	0.2	1.4	0.19
	(n=4) SD	1	4	0.5	2	1	0.2	1	0.2	0.7	0.2	0.5	0.07	0.4	0.06
	merrillite	35	99	12	57	18	1.1	19	4	28	5.5	14	2.1	11	1.8
	(n=3) SD	4	23	1	7	3	0.3	3	1	2	0.7	2	0.3	2	0.4
Allegan	merrillite	48	129	19	88	28	1.8	37	6	43	9	28	3.8	24	3.3
	(n=5) SD	7	22	4	18	6	0.3	8	2	10	2	7	0.9	6	0.9
Portales Valley	apatite	4	9	1	4	1	0.9	0.9	0.12	0.8	0.2	0.5	0.07	0.4	0.07
	(n=3) SD	1	3	0.4	1	0.3	0.1	0.4	0.08	0.3	0.1	0.2	0.02	0.1	0.03
	merrillite	28	74	10	47	14	1.7	15	3	19	4	12	2	15	2.1
	(n=7) SD	1	3	0.6	3	1	0.2	1	0.2	1	0.3	1	0.2	1	0.2
Aguemour 009	merrillite	76	215	32	147	44	2.4	51	9	59	13	37	4. 9	30	3.9
	(n=3) SD	3	7	1	6	3	0.1	3	0.4	5	0.8	3	0.2	2	0.3
Bruderheim	apatite	28	46	5	20	3	0.8	3	0.5	3	0.7	2.2	0.3	2.2	0.3
	(n=7) SD	1	2	0.4	2	1	0.1	1	0.1	0.4	0.1	0.4	0.07	0.4	0.1
Villalbeto	apatite	18	39	5	20	5	1.3	6	0.86	5	1	2.9	0.38	2.3	0.3
de la Peña	(n=4) SD	1	1	0.2	1	0.5	0.1	0.5	0.05	0.5	0.1	0.2	0.03	0.3	0.1
	merrillite	81	224	31	142	42	1.9	55	10	62	14	38	5.2	32	4.8
	(n=10) SD	15	68	8	26	9	0.3	12	2	15	3	9	1.2	7	1
Adzhi-Bogdo	apatite	18	40	5	22	6	1.2	6	1	6	1.3	4	0.5	2.7	0.34
(chondritic portion)	(n=5) SD	2	2	0.3	2	0.4	0.2	1	0.1	1	0.2	0.3	0.05	0.4	0.04
	merrillite	101	275	41	200	62	2.7	84	15	93	20	54	6.7	39	5
	(n=5) SD	9	36	5	25	8	0. 6	8	2	13	3	9	1.2	7	1
Adzhi-Bogdo	apatite	50	125	17	79	25	1.7	27	6	38	9	28	4.5	30	4.5
(differentiated clasts)	(n=3) SD	8	26	4	15	5	0.3	3	1	6	2	5	0.7	5	0.9
	merrillite	63	236	39	176	65	6	90	15	107	23	67	9.4	52	6.4
	(n=2) SD	5	16	5	17	5	0.1	4	1	4	2	5	0.5	4	0.8
Karoonda	apatite	11	38	5	16	4	1.3	3	0.7	3.3	0.6	1.5	0.2	1.3	0.2
	(n=3) SD	1	8	1	3	1	0.1	1	0.1	0.6	0.1	0.1	0.02	0.4	0.04
Acapulco	apatite	56	125	15	64	17	1	20	3	21	4	11	1.3	8	1.0
	(n=9) SD	7	15	2	11	4	0.1	4	1	5	1	3	0.3	1	0.2
	merrillite	90	236	32	140	43	1.8	55	10	66	15	41	5.5	36	4.8
	(n=7) SD	21	63	11	62	23	0.1	31	5	34	7	18	2.0	13	1
Dhofar 125	apatite	60	115	14	60	19	1.4	28	5	39	9	27	3.4	19	2.6
	(n=4) SD	16	26	4	16	4	0.2	6	0.9	7	2	3	0.3	2	0.3
NWA 1052	merrillite	29	54	6	25	7	1.5	12	2	18	4	14	2.1	17	2.3
	(n=3) SD	11	19	2	9	4	0.04	5	1	10	2	7	1.2	5	0.9
HaH 193	apatite	13	32	4	20	6	0.7	8	1	9	2	6	0.9	7	1.8
	(n=8) SD	11	21	2	10	3	0.2	4	0.7	5	1	3	0.5	4	0.7
NWA 5073	apatite	545	1852	273	1369	417	3.6	482	76	455	89	225	28	175	22
	(n=3) SD	482	1421	228	1174	328	2	374	55	307	57	127	14	76	8
Millbillillie	apatite	99	280	43	201	62	2	69	12	75	15	41	5.4	37	5
	(n=3) SD	15	22	4	34	13	0.4	15	3	16	2	7	0.7	8	1
	merrillite	4856	11571	1702	8871	2597	19	3501	553	3184	686	1791	224	1267	176
	(n=2) SD	117	599	80	179	48	1	361	26	125	19	25	12	10	8
SaU 005	merrillite	14	46	8	59	49	13	100	20	132	28	75	10.12	64	8.7
	(n=3) SD	1	4	1	5	2	1	8	1	8	2	6	0.80	3	0.4
DaG 1051	merrillite	17	55	10	77	62	15	137	27	180	37	99	12.6	76	10
	(n=5) SD	2	5	1	9	8	1	17	3	21	4	10	1.1	6	1
NWA 4864	apatite	100	250	36	175	69	18	109	19	126	26	71	9.2	60	8
	(n=3) SD	8	16	2	13	6	3	9	1	7	2	6	1.3	10	1
	merrillite	118	312	42	190	73	25	111	21	142	30	80	10.4	66	9
	(n=4) SD	11	35	4	25	9	1	13	2	12	2	6	0.6	4	0.5
KG 002	merrillite	163	417	59	288	109	32	165	30	191	39	103	13	77	10
	(n=4) SD	13	43	6	33	12	2	20	3	15	3	6	0.6	3	1
Zagami	merrillite	61	126	16	68	68	1.5	19	3	18	4	10	1.3	8	1.1
	(n=11) SD	2	11	1	2	18	0.1	1	0.2	0.5	0.2	0.5	0.1	0.3	0.2
ALM-A	apatite	23	66	10	49	15	71	20	3	24	5	16	2	15	2.1
	(n=6) SD	3	13	2	9	2	11	20	0.4	3	1	2	0.3	2	0.3
Dalgaranga	merrillite	42	121	18	85	27	6	31	5	33	7	19	2.5	16	2.3
	(n=5) SD	6	20	3	12	4	0.4	8	1	8	2	5	0.6	3	0. 6
Bondoc	merrillite	5	19	3	18	6	1.5	9	2	11	2	7	1	7	1.1
	(n=12) SD	0.1	1	0.2	1	0.4	0.05	1	0.1	1	0.2	0.5	0.04	0.2	0.02
Landes	apatite	3	13	2	11	4	1.5	4	0.7	5	1	3	0.4	4	0.48
	(n=2) SD	0.02	0.1	0.05	0.4	0.1	0.02	0.1	0.02	0.3	0.07	0.1	0.007	0.2	0.02
	merrillite	12	25	3	11	2	1.9	3	0.5	3	0.6	2	0.25	1.7	0.20
	(n=2) SD	1	1	0.3	1	0.4	0.2	0.1	0.1	0.5	0.06	0.2	0.04	0.4	0.03

1394

Figures

Figure 1

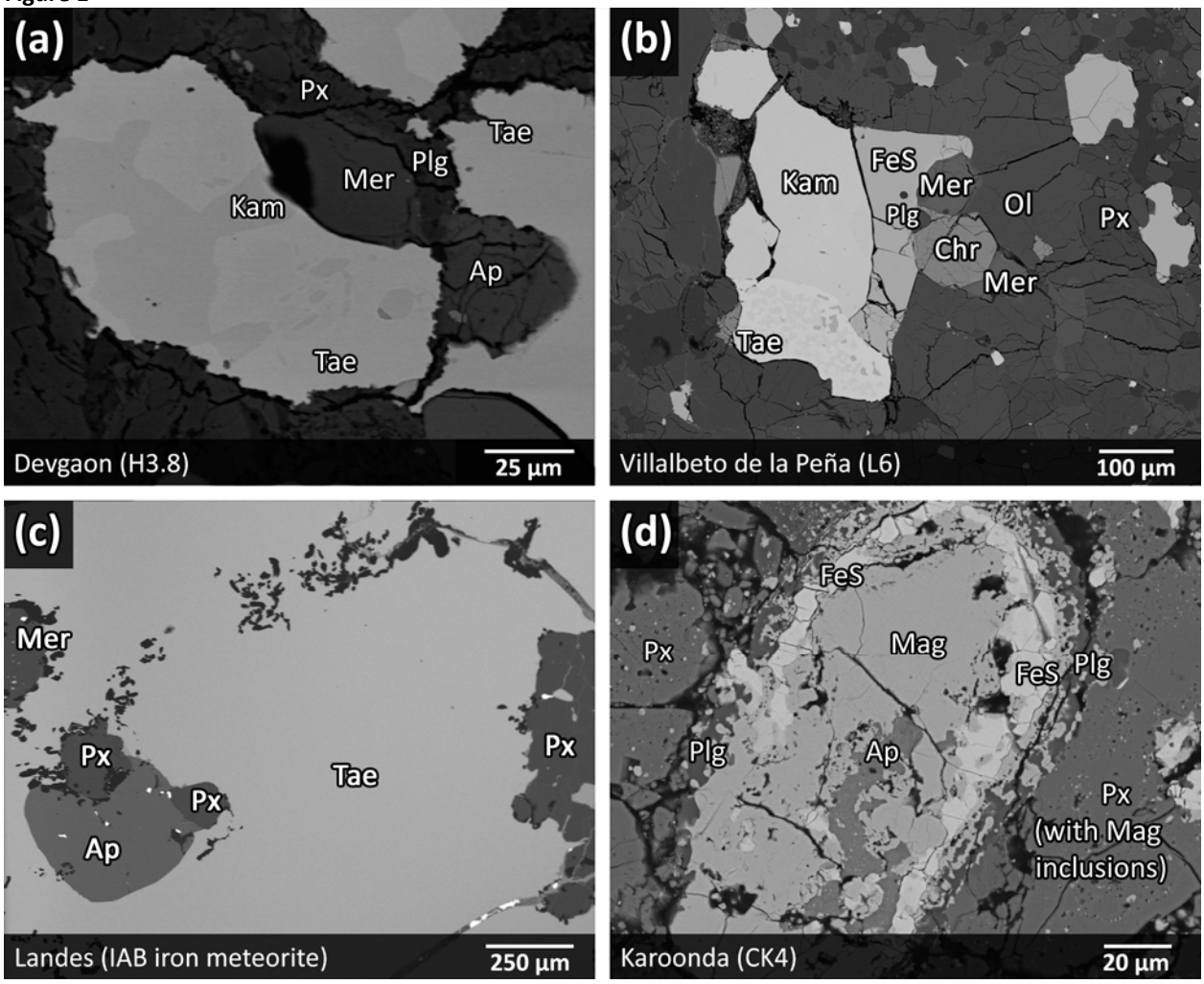

1399 **Figure 2**

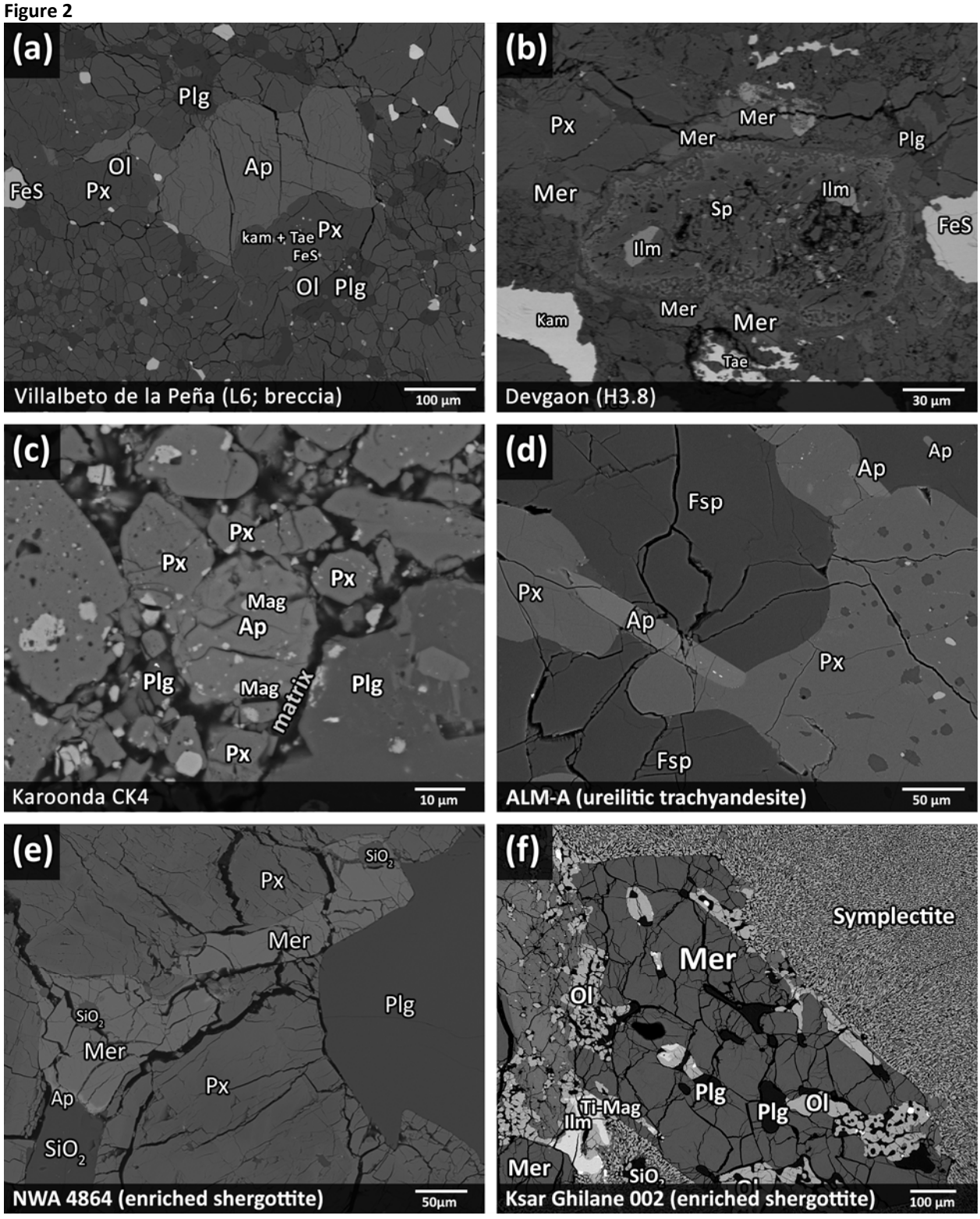

1400
1401

1402 **Figure 3**

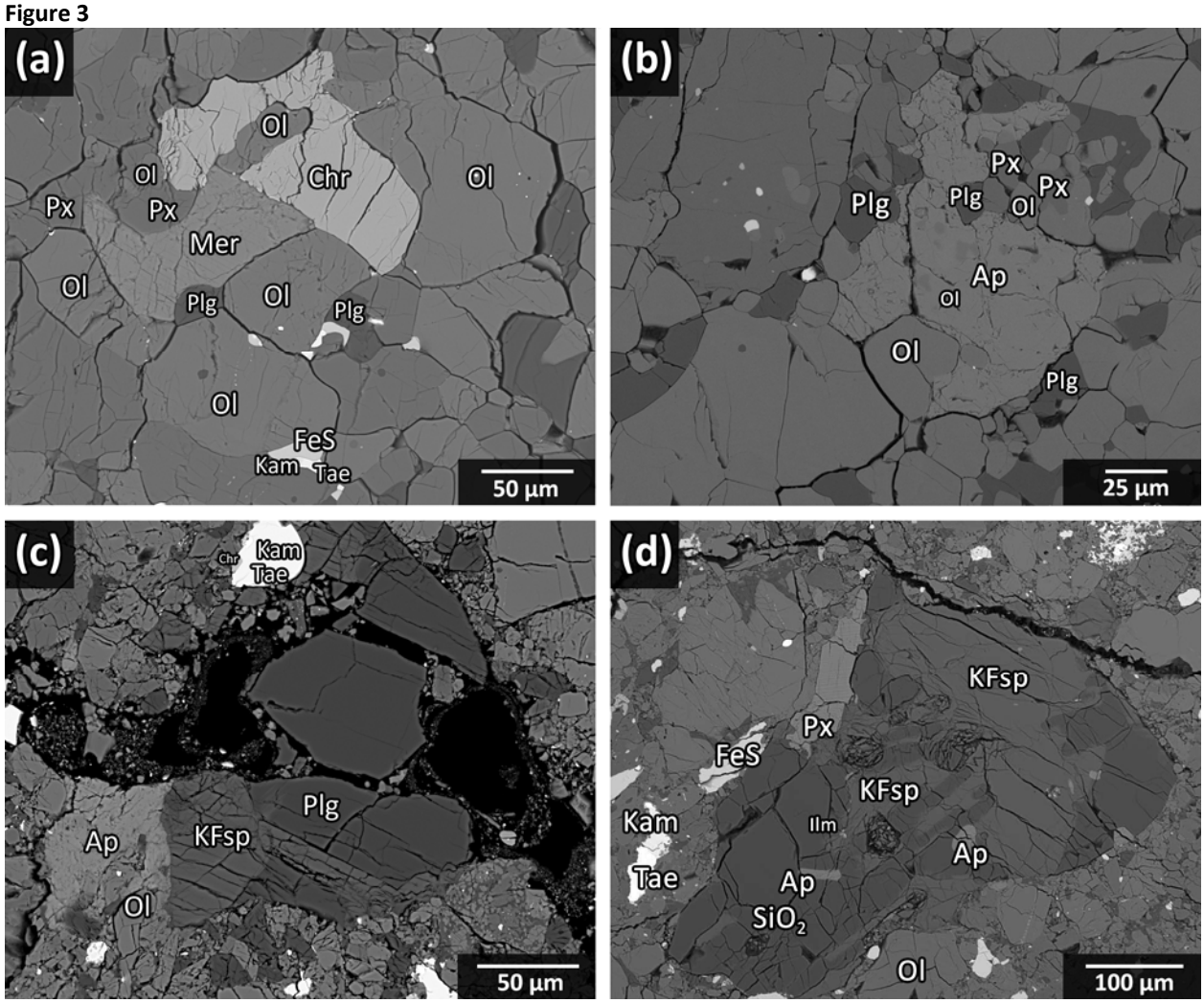

1403
1404

1405 **Figure 4**

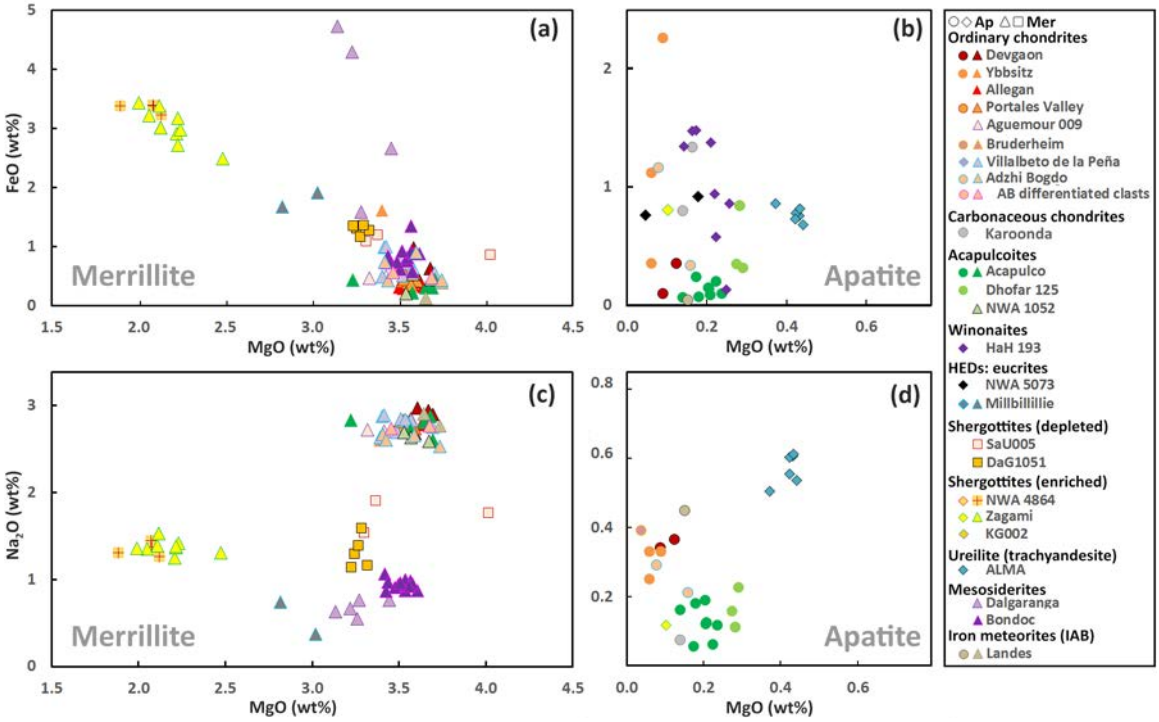

1406

1407 **Figure 5**

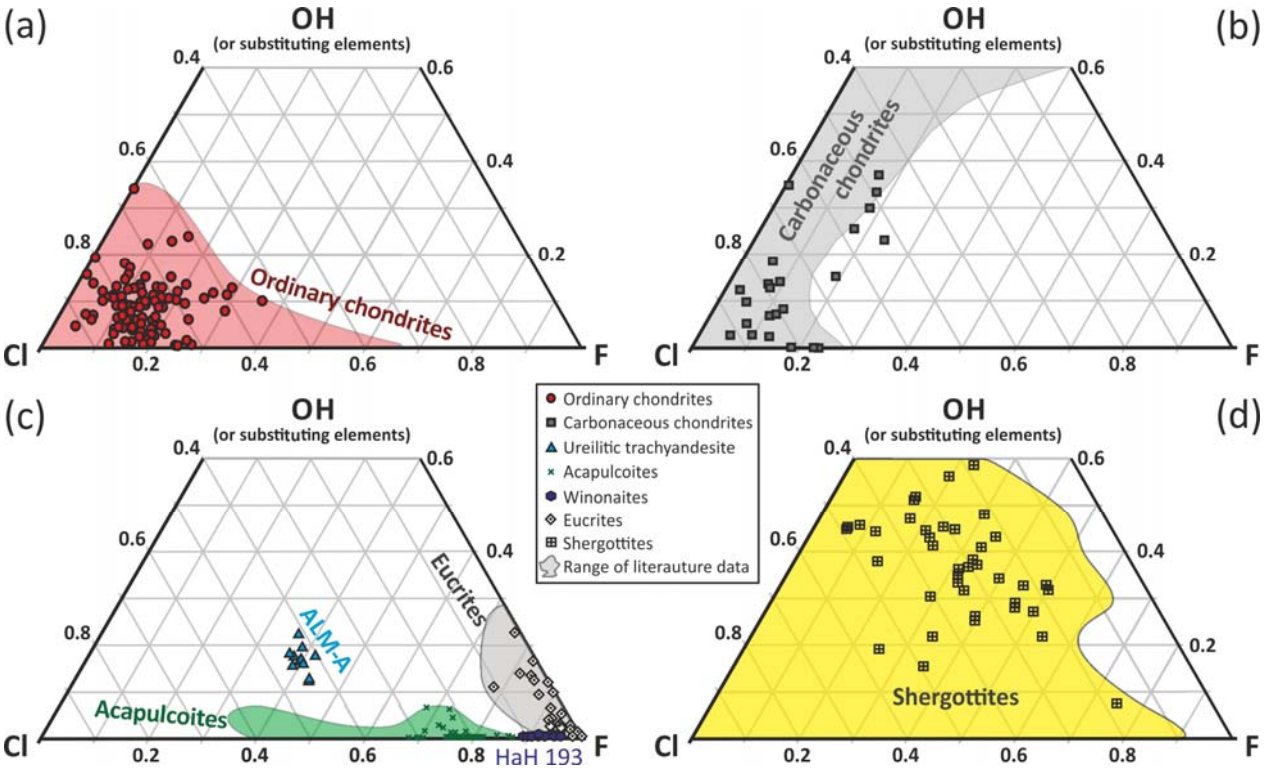

1408

1409 **Figure 6**

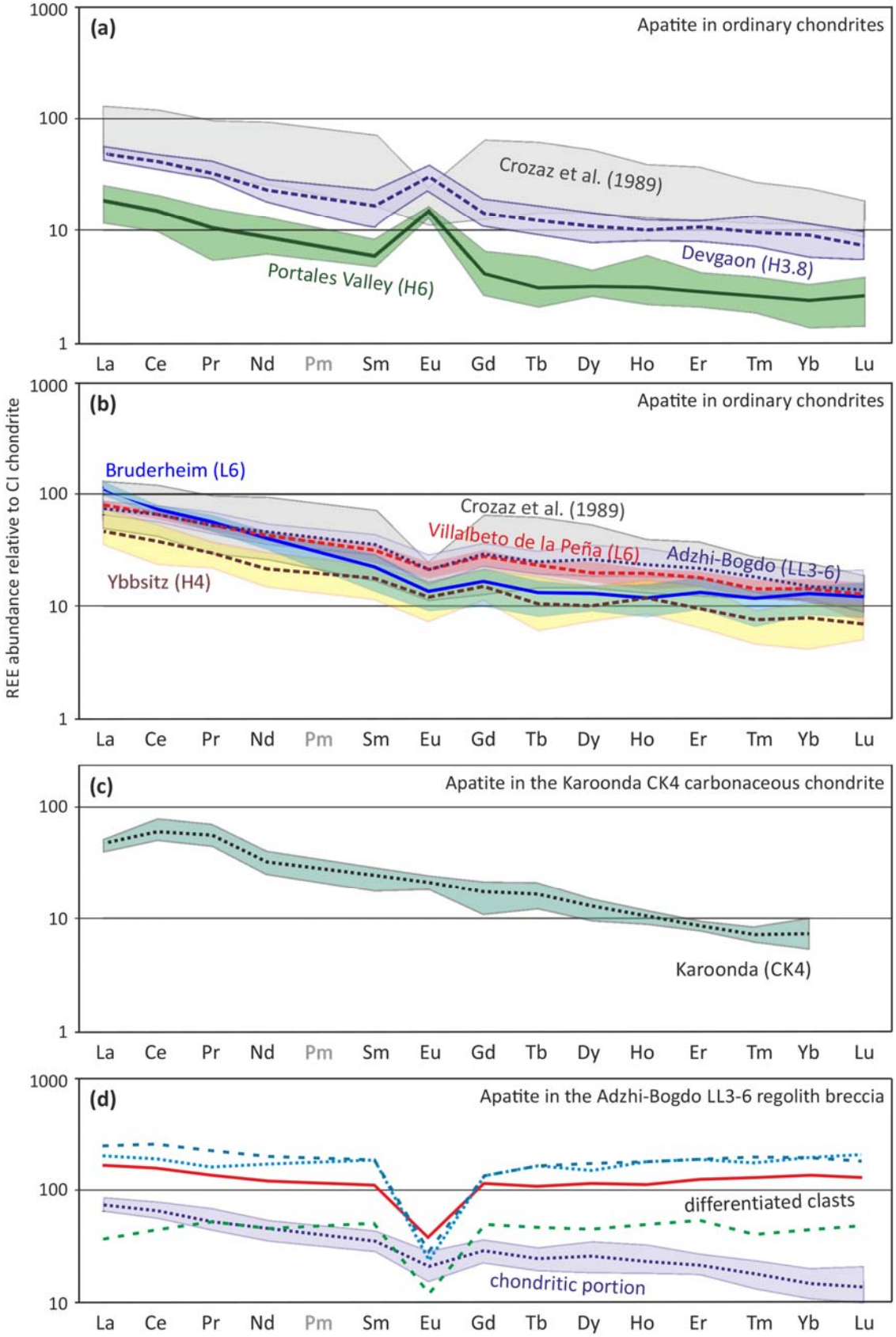

1410

1411 **Figure 7**

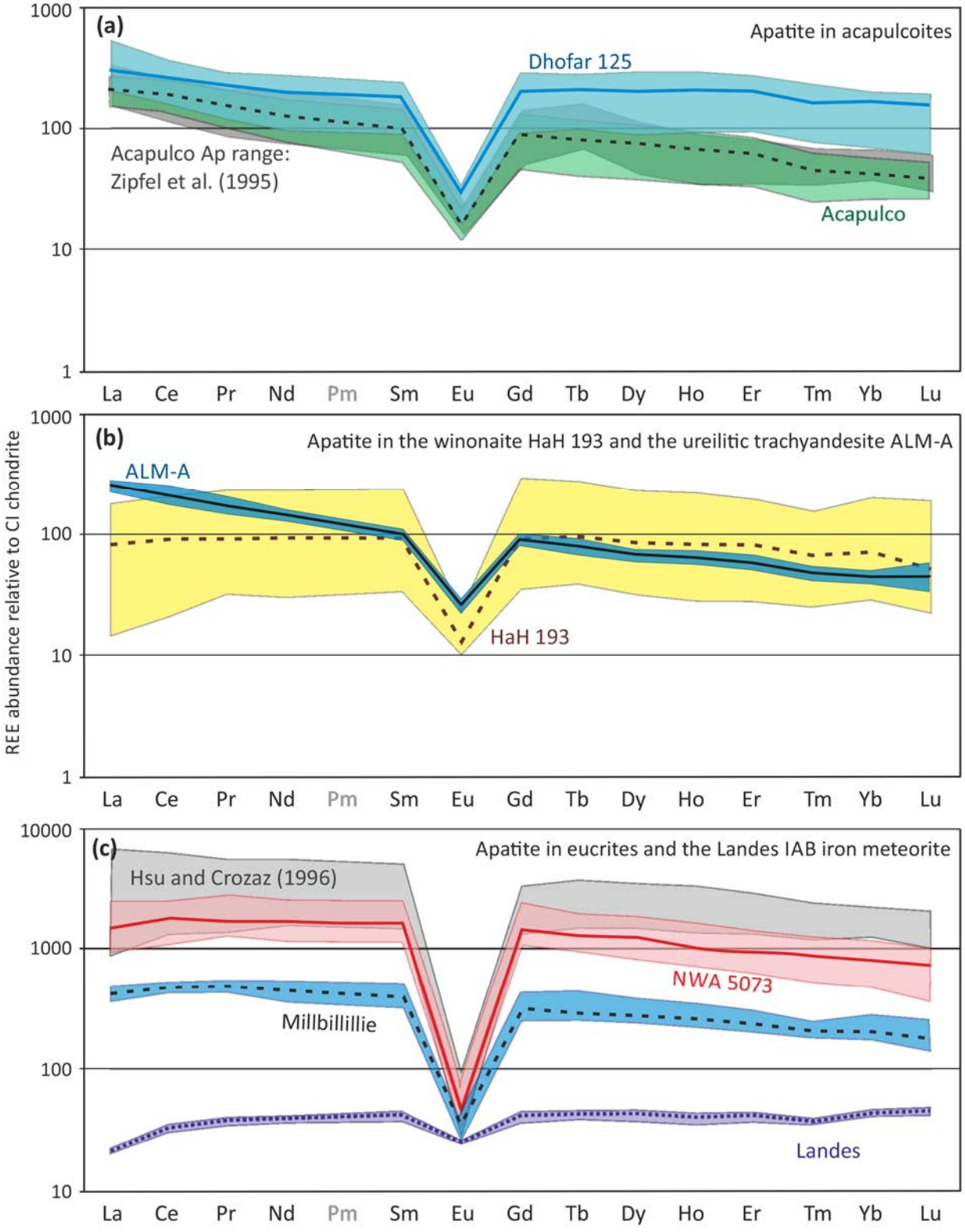

1412
1413

1414 **Figure 8**

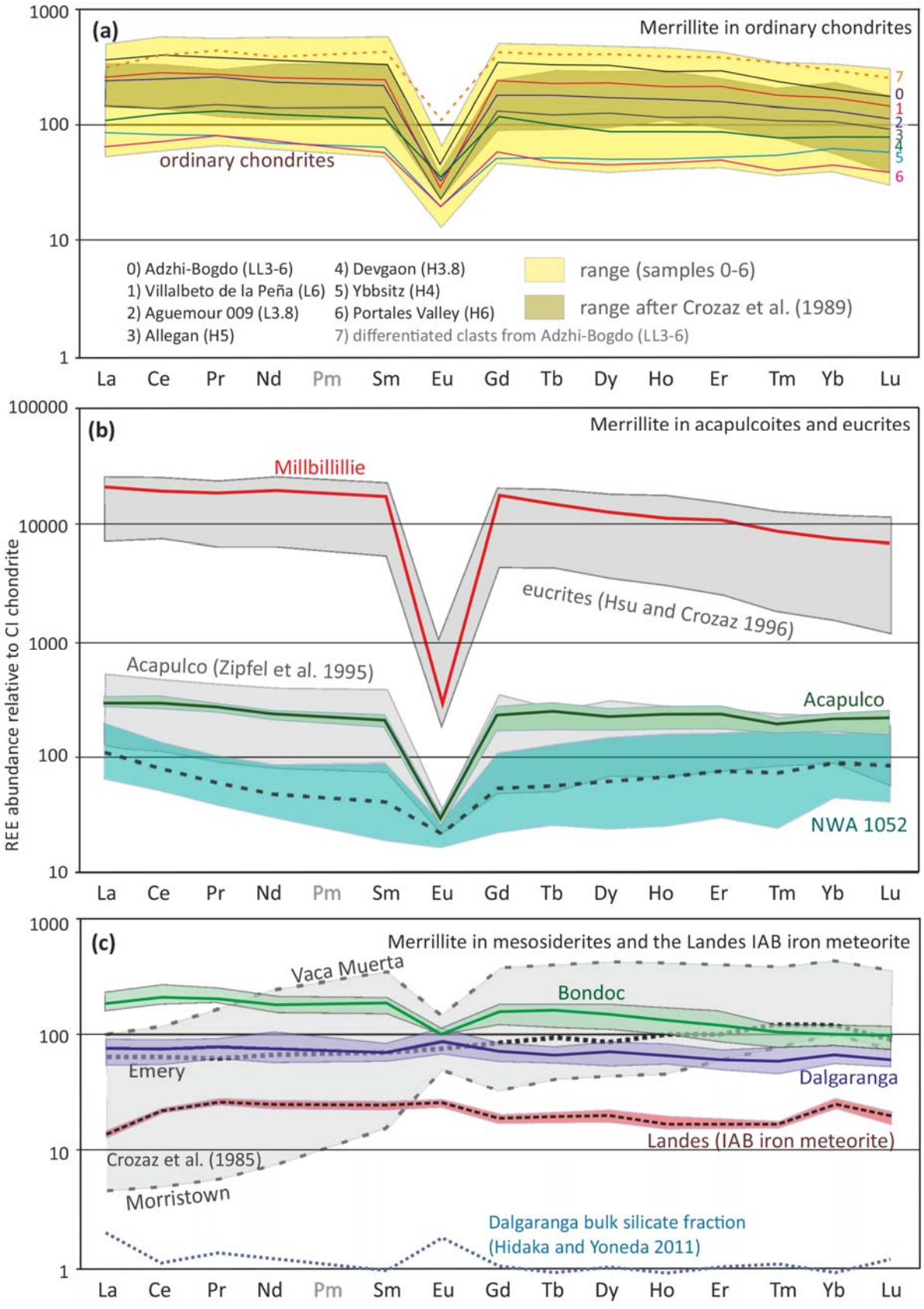

1415

1416 **Figure 9**

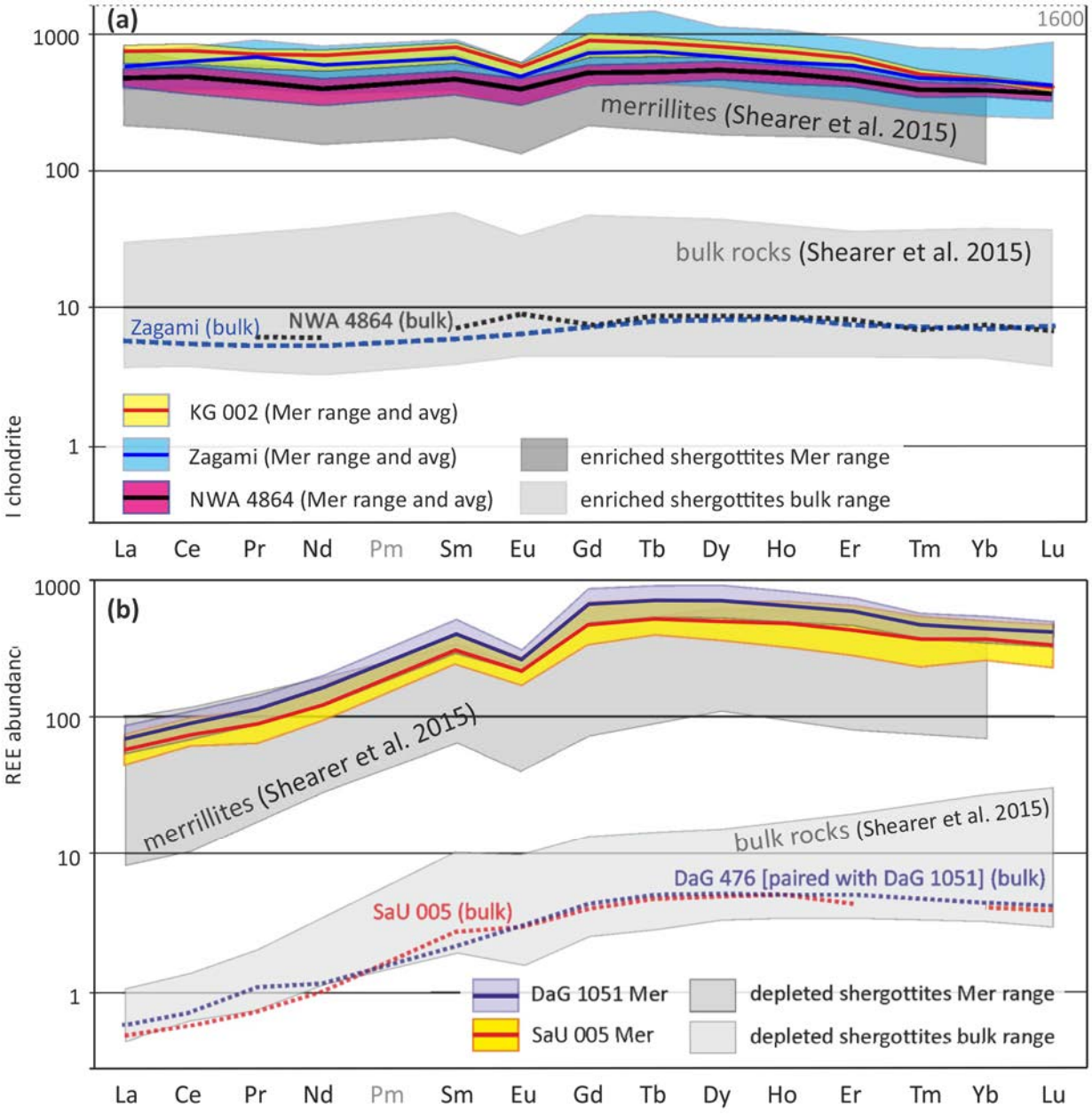

1417

1418

1419 **Figure 10**

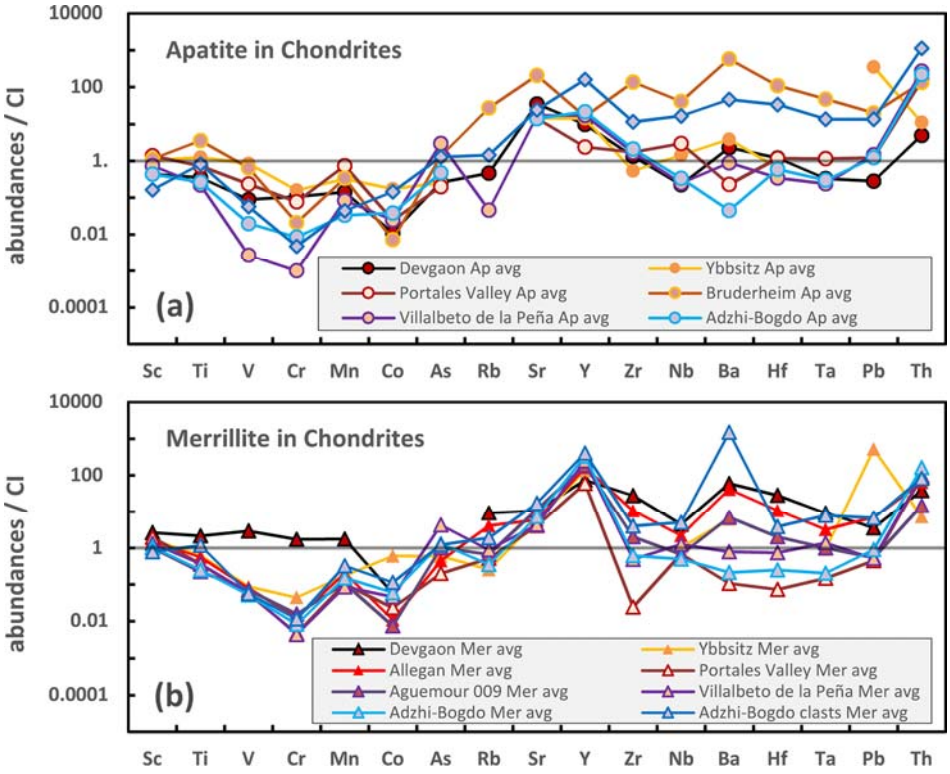

1420

1421 **Figure 11**

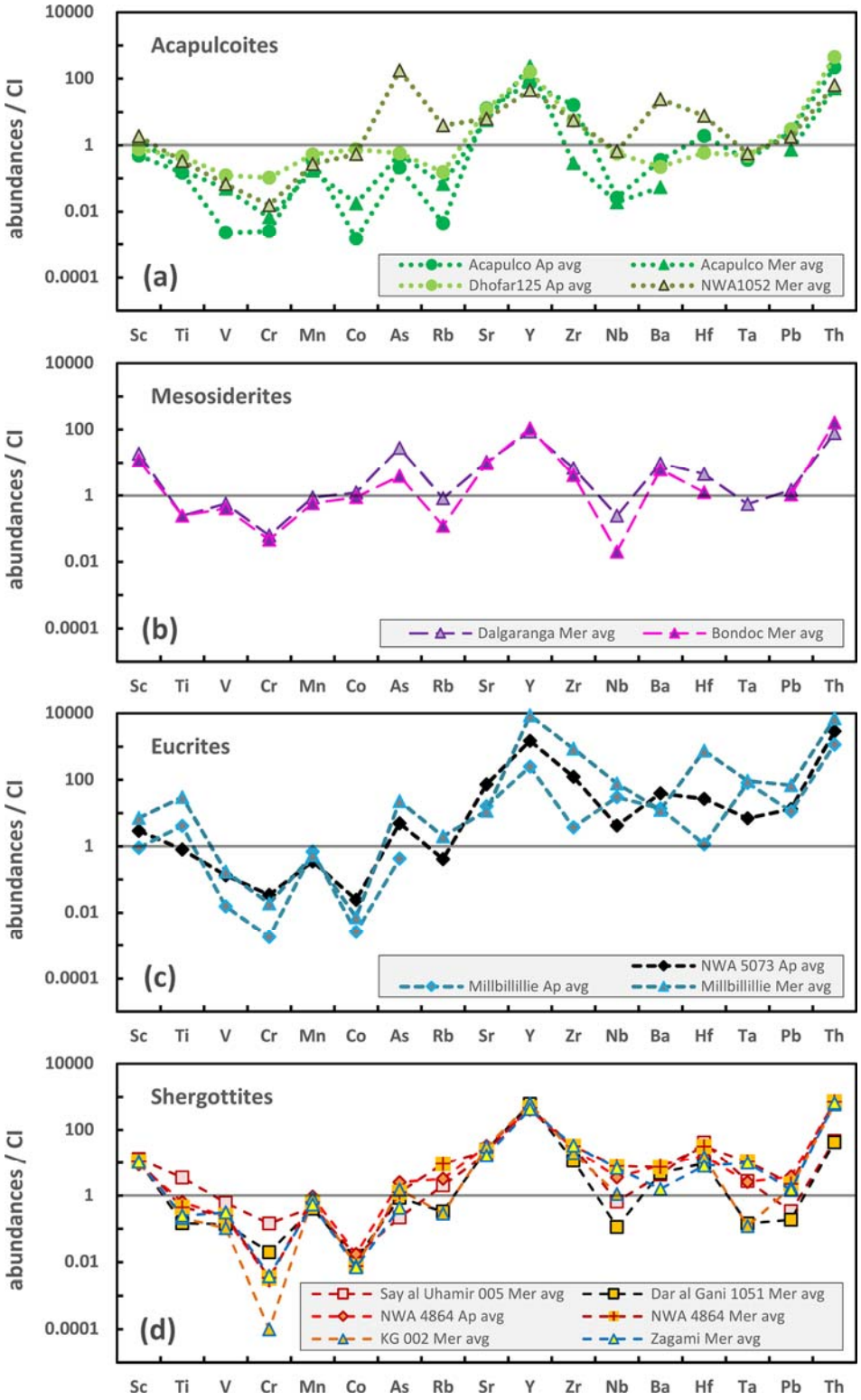

1422

1423

1424 **Figure 12**

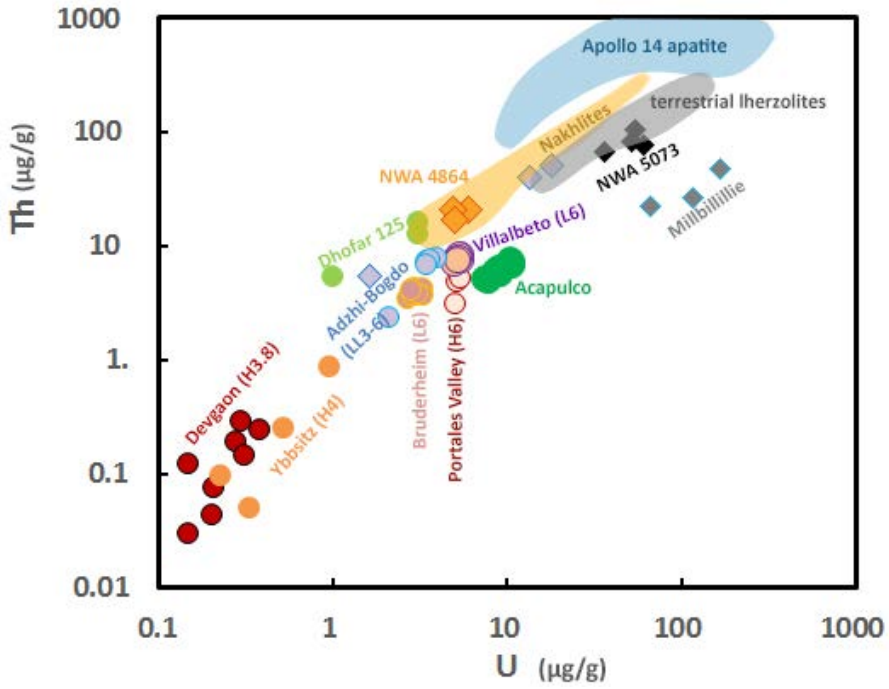

1425

1426 **Figure 13**

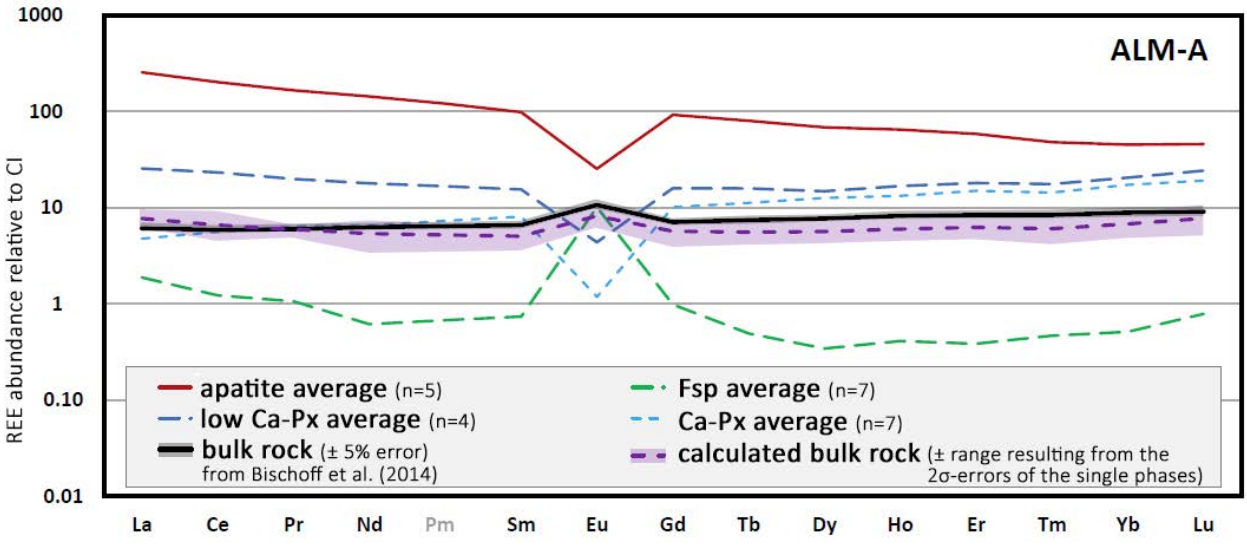

1427

1428

1429